STRAIN-CONTROLLED IMPURITY-INDUCED DISORDERING FOR APERTURES IN SINGLE-MODE VERTICAL-CAVITY SURFACE-EMITTING LASERS

BY

PATRICK SU

THESIS

Submitted in partial fulfillment of the requirements
for the degree of Master of Science in Electrical and Computer Engineering
in the Graduate College of the
University of Illinois at Urbana-Champaign, 2019

Urbana, Illinois

Adviser:

Professor John M. Dallesasse

ABSTRACT

Vertical-Cavity Surface-Emitting Lasers (VCSELs) have become ubiquitous in modern consumer markets. Owing to their small footprint, circular-beam profile, on-wafer probing capability, and high reliability, VCSELs have been widely deployed for data communication transmitters and position sensors. In the advent of emerging applications such as autonomous driving and 3-D facial recognition systems, high-power 2D VCSEL arrays are being used as the premier illumination device for time-of-flight (ToF)-based light detection and ranging (LIDAR) optical sensors.

Through the initiation of Zn diffusion, impurity-induced disordering (IID) has been demonstrated to enable optical mode control, increased modulation frequencies, and provide carrier and photon confinement in vertical-cavity surface-emitting lasers. While disordering provides a wafer-scale method of improving device performance, the regions of disordering must be carefully controlled. Adverse effects can overshadow the benefits of disordering if it is not properly managed. Due to the isotropic nature of diffusion, undesirable lateral undercutting can occur during deep disordering processes where the severity of this effect is defined by the initial diffusion front formed.

In this work, the fine control of Zn diffusion fronts in apertures formed using impurity-induced disordering is presented. By tailoring the diffusion mask strain, the diffusion front curvature of the impurity-induced disordering aperture can be controlled. Through modifying the composition of SiN_x diffusion masks, various film stresses can be achieved. When employed for disordering, these form a variety of disordering apertures with differing diffusion fronts. These distinct impurity-induced disordering apertures are characterized for their lateral-to-vertical diffusion front ratios and an analysis and discussion of the physical mechanisms is presented The demonstration of this work enables more sophisticated and precise disorder-defined apertures for high-performance VCSELs.

To my family, for their love and encouragement

ACKNOWLEDGMENTS

The completion of this work would not have been possible without the contributions of several individuals whom I feel thankful to call my family, friends, and mentors. First, I would like to express my love and gratitude towards my family, whom have always been at the foundation of my life. Their unconditional guidance, support, and encouragement are more than I deserve and enabled the completion of this work.

I am proud and thankful of being born and raised in town of Geneva, Illinois. To Cody Murphy, Doug Davis, and Thomas Schleich, I thank you for our shared companionship and life-long memories of which I cherish daily, despite being away far too often. To Collin Schumock, Josh Perozek, Kevin Nadro, Brittany Joy, Amanda (Ebert) Murphy, and the entire Murphy and Davis families, I thank you for your friendship, hospitality, and memories.

I am fortunate to have had many mentors that have led me to pursue the field of optoelectronics as well as the completion of this work. I am grateful and indebted to Thomas O'Brien, Jr. for laying the foundation of this work and being under his tutelage. I would also like to thank Benjamin Kesler, Fu-Chen Hsiao, Kanuo Chen, John Carlson, Saoud Al-Mulla, and Josh Perozek for their insightful discussions regarding device physics, modeling, and semiconductor fabrication. I would also like to thank Robert Kaufman for his assistance with diffusion mask images and experiments.

Lastly, and foremost, I would like to give my immense gratitude towards my adviser, Professor John Dallesasse. His advisement, wisdom, and patience, for many years, is something that I feel fortunate of receiving and has been the basis of my knowledge, intuition, and enthusiasm towards the field of optoelectronics.

TABLE OF CONTENTS

LIST OF ABBREVIATIONS

DBR	Distributed Bragg Reflector
HOM	Higher-Order Modes
IID	Impurity-Induced Disordering
LIDAR	Light-Detection and Ranging
L/V	Lateral-to-Vertical
SEL	Surface-Emitting Laser
TOF	Time-of-Flight
VCSEL	Vertical-Cavity Surface-Emitting Laser

CHAPTER 1

INTRODUCTION

1.1 Historical Development of Vertical-Cavity Surface-Emitting Lasers (VCSELs)

Early demonstrations of a surface-emitting laser (SEL) was achieved by Melngailis in an InSb diode structure in 1965 [1] and in an InGaAsP/InP double-heterostructure by Soda and Iga in 1979 [2]. Largely attributed to the early use of metallic layers for optical reflectors and poor overlap between the electric-field pattern with the gain region, the threshold of these devices was far too large for any practical applications.

Even with further development of surface emitting lasers, they did not evolve into the modern low threshold and low power consumption form until several technological breakthroughs were developed. The first was the adoption of distributed Bragg reflectors (DBR) demonstrated by Scifres and Burnham in 1975 [3]. This enabled the formation of highly reflective mirrors (R $\approx$ 99%) through repeatedly layering alternating high and low index material grown to quarter-wavelength thicknesses. While this was a significant improvement, it was not until the discovery of native oxide growth in $Al_xGa_{1-x}As$ layers by Dallesasse and Holonyak in 1989 [4] and its application to a VCSEL structure by Huffaker and Deppe in 1994 [5] that enabled energy-efficient and reliable performances with record-low thresholds. The use of an oxide aperture not only provides enhanced carrier and optical confinement, but also greatly reduces the active device diameter, thereby achieving continuous-wave room-temperature operation with sub-milliampere lasing thresholds.

1.2 Introduction of VCSELs in Consumer Markets

Since the incorporation of the oxide-aperture, VCSELs became widely deployed for optical links in data centers. Due to the demand of growing global data center traffic as shown in Fig. 1.1, faster and more energy-efficient interconnects grew correspondingly with the emergence of datacentric applications such as cloud storage, artificial intelligence, and autonomous driving.

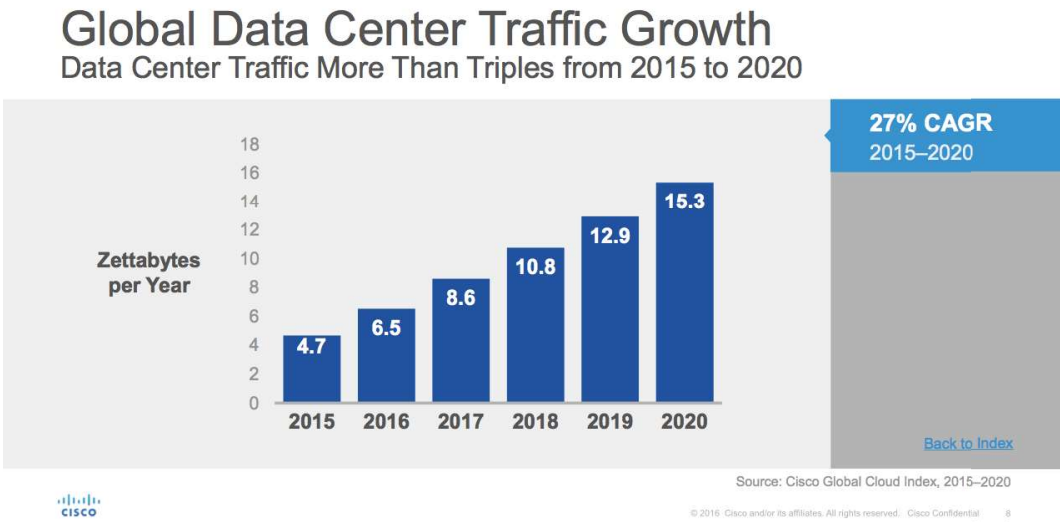

Figure 1.1: Forecast growth of data center traffic by Cisco Systems (2015 - 2020) from [6].

The advancements of data center links growing toward and beyond gigabit per second speeds began to prove copper interconnects were no longer a viable solution for longer transmission lengths. Traditional copper cables become highly attenuating at either GHz modulation speeds or over longer lengths than optical fiber cables whereas the major advantage of copper cabling over optical fibers was primarily lower costs [7].

However, the increased utilization of VCSELs in data centers garnered interest to improve the manufacturability and performance of VCSELs over many years that was complimented with other supplementary technologies for low-cost optical links. Due to its well-established manufacturing ecosystem, in addition to its unique energy-efficient performance, VCSELs became poised for success as a premier solution for next-generation optical links in addition to emerging applications such as optical 3-D sensing.

1.3 High-Power Single-Mode VCSELs for Optical 3-D Sensing

In the advent of emerging applications such as 3-D optical mapping that commonly utilize light detection and ranging (LIDAR) systems [8], development of optical emitters capable of spanning a wide area for 3-D mapping began to attract a large interest. As illustrated in Fig. 1.2, the high-density textured point clouds can be synthesized into a high-resolution 3-D rendering of environmental surroundings. This has found utility for consumer applications such as 3-D facial recognition and autonomous driving systems.

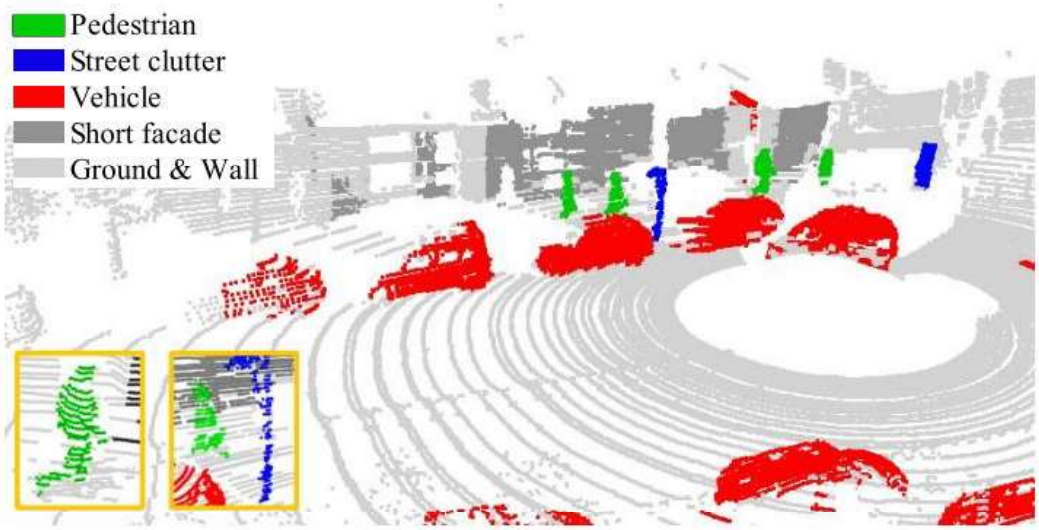

Figure 1.2: Illustration of LIDAR point cloud mapping of vehicles and pedestrians from [9].

Due to the maturity and compactness of semiconductor-based solutions, VCSELs have been widely successful in time-of-flight (ToF) -based LIDAR systems. ToF-based LIDAR systems utilize pulsed VCSEL arrays with relatively low duty cycles and measure the time-delay of the returning signal corresponding to the distance, velocity, and surface characteristics of a target object. Due to the strong background noise in addition to attenuation effects over long propagation distances, several watts of power can be necessary for operating ranges up to 100 m [8]. While VCSELs have been limited up to hundreds of milliwatts under continuous-wave operation, pulsed-operation of these devices have led to 10-W of peak maximum power [10]. Furthermore,

the structure of a VCSEL enables the capability of being formed into a compact array. As a result, 2-D arrays of VCSELs have been demonstrated to emit at 1.55 W for 19 elements when proper heat-sinking is applied [10]. A top-down view of a 2-D VCSEL array alongside a scanning-electron microscope (SEM) cross-section is shown in Fig. 1.3 to provide a visual representation of a 2-D VCSEL array.

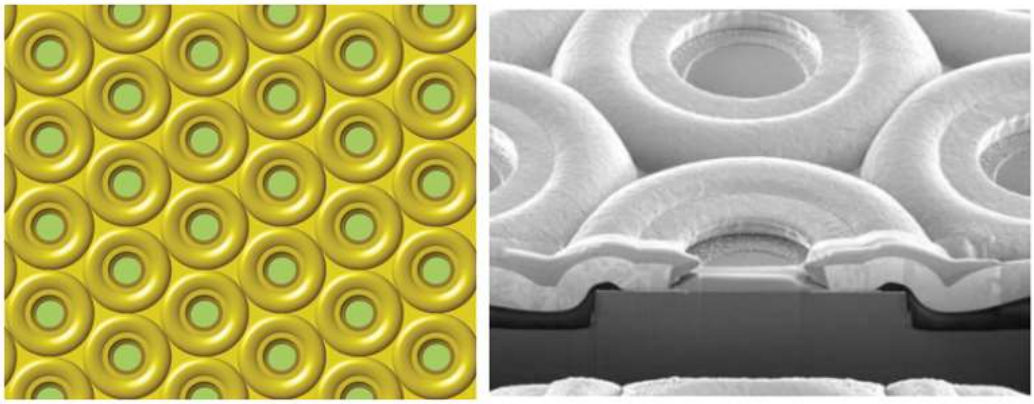

Figure 1.3: Top-side image of a metallized 2-D VCSEL array (left) with SEM cross-section (right) shown from [11] and [12] respectively.

The aperture sizes reported from [10] range from 170 to 320 um in active diameter which greatly supports a number of higher-order modes. Since all of these modes have different effective mode indexes, they also propagate at slightly different speeds with different energies commonly referred to as modal dispersion. For ToF-based LIDAR systems, it is ideal to have a single propagation velocity and a well-defined photon energy. This allows the detector to distinguish a well-defined signal from background noise. As a result, single-mode operation of high-power 2-D VCSEL arrays is greatly desired. Single-mode signals have been shown to be less divergent and more coherent than their multi-mode counterparts. However, methods that demonstrate single-mode operation either require complex fabrication processes that are difficult to scale or employ low-yield, high-cost regrowth processes which prohibit its use for high-volume manufacturing.

This work presents on a scalable method of achieving single-mode high-power operation in VCSELs which is achieved via impurity-induced disordering (IID). Impurity-induced disordering is a physical phenomenon that intermixes the AlGaAs-based distributed Bragg reflector (DBR) functioning as optical mirrors in VCSELs. Consequently, the disordered regions of

the DBR exhibit lower power reflectivity. When the disordering is designed to overlap primarily the higher-order modes while relatively unaffecting the fundamental-mode, single-fundamental-mode operation can be achieved through higher-order mode suppression. This work will present the modal-behavior analysis of IID VCSELs for various disordering aperture sizes that function as a higher-order mode filter. An analysis and discussion of the modal-behavior will be presented that motivates the necessity for finely-tuned disordering apertures. By modifying the strain of the diffusion mask, the capability of tailoring the disordering is achieved. As a result, distinctly different disordering apertures defined by their diffusion fronts will be shown and a discussion of the underlying physical mechanisms will be discussed.

CHAPTER 2

FUNDAMENTALS FOR SINGLE-MODE VCSELS

2.1 Oxide-Confined VCSEL

The modern VCSEL structure consists of distributed Bragg reflectors (DBR) for highly reflective optical mirrors surrounding an active region composed of several quantum-wells for high gain efficiency, and a confinement aperture placed near the active region [13, 14, 15]. As demonstrated by many [5, 13], an oxide-aperture greatly enhances the optical and carrier confinement through the active region of the device. Thus, a confinement aperture in the form of either native oxide [5, 8, 11, 12, 13, 16, 17] or proton implantation [18, 19] is widely used by many, leading to low threshold and energy efficient operation in modern VCSELs. Due to its cost-efficient growth and lattice-matched material system, AlGaAs/GaAs has proven to be one of the most common VCSEL compositions currently deployed for a wide variety of applications and will be the main material system presented in this work.

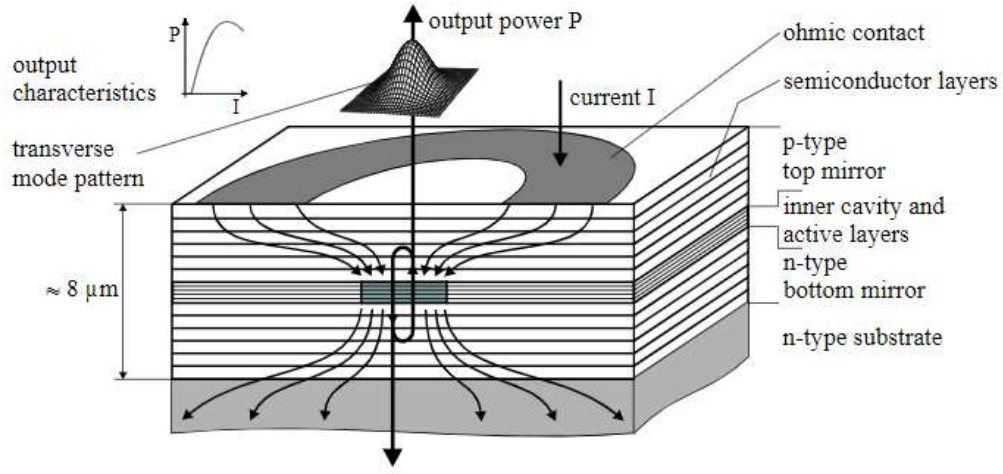

Figure 2.1: Schematic of an oxide-confined VCSEL from [20].

Starting from the bottom of the VCSEL structure in Fig. 2.1, the substrate of a VCSEL is typically either n-type or semi-insulating (SI) followed by subsequently grown n-DBR pairs. Then comes the active region that consists of the several quantum-wells surrounded by cladding layers for optical mode confinement. Single or double high-aluminum content layers are then placed several layers above the active region to enable oxide aperture formation during the fabrication process. In the illustration of Fig. 2.1, the current is confined through the center of the gain media that results in a higher current density achieved for a given current injection. This allows the current threshold density to be met at lower current injection levels compared to non-confined VCSELs. While other high-aluminum content layers, notably $Al_{0.96}Ga_{0.04}As$, may be placed to reduce parasitic capacitance for high-speed applications [21, 22], the lateral oxidation rate increases by orders of magnitude from $Al_{0.96}Ga_{0.04}As$ to $Al_{0.98}Ga_{0.02}As$ [13, 23]. Therefore only the high-aluminum content layer will predominantly define the carrier and optical confinement of the device.

2.2 Methods of Mode Control in VCSELs

As depicted in Fig. 2.1, the optical cavity is confined only between the active region and cladding layers since both DBR layers effectively function as optical mirrors and do not contribute toward the optical cavity length. As a result, small optical cavity lengths in the longitudinal direction which leads to single-longitudinal-mode operation without any further modifications is a unique benefit of VCSELs. The transverse dimension, however, typically spans several wavelengths that leads to multiple-transverse mode operation. On the other hand, the oxide aperture electrically and optically passivates the oxidized regions as an electrical insulator and low refractive index material respectively; thus reducing the active device diameter and number of supported transverse modes. Since the reduced active device diameter also reduces the number of supported optical transverse modes, the oxide-aperture provides a method of reducing the number of supported optical modes by reducing aperture size until all higher-order modes (HOM) are suppressed.

Single-mode operation through reducing the oxide-aperture size has been

reported in literature [24], however, the immense reduction of the active diameter of the device concurrently led to self-heating, lower output powers, and shorter device lifetimes [25]. More intricate methods of optical mode control have therefore been developed and adopted.

When the optical mode profile in a VCSEL is examined, a simplified method is to approximate the VCSEL structure as a two-layer dielectric waveguide. Invoking the assumption that the oxide-aperture predominantly defines the supported optical modes propagating in a VCSEL, the optical modes can be numerically calculated using the two-layer circular dielectric waveguide model with the oxide aperture set as the outer dielectric layer. Since the layers are not metallic and the field must be continuous at the dielectric interface between core and cladding, only hybrid electromagnetic modes can satisfy the wave equation. A more rigorous derivation is provided in reference [26].

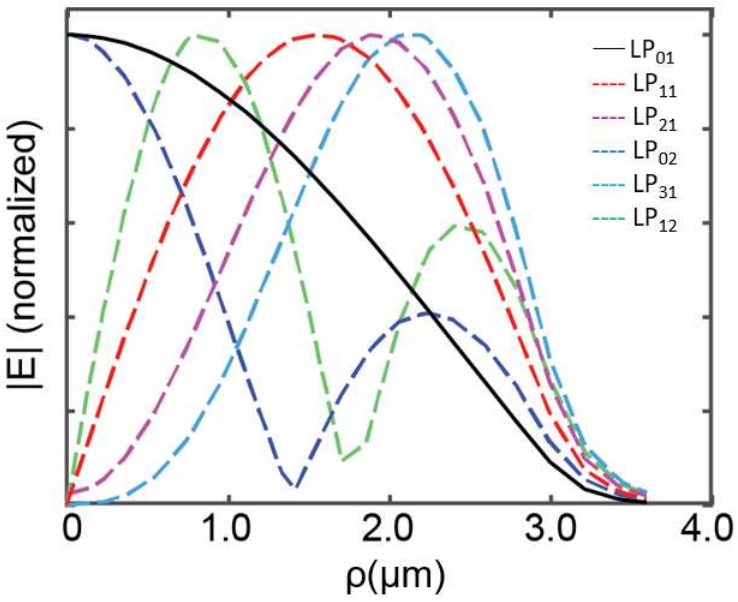

Figure 2.2: Optical mode profile of various modes supported in a VCSEL using the weakly guiding approximation in a two-layer circular dielectric waveguide model [27].

The radial profile of the fundamental mode can be plotted along with the corresponding higher-order modes shown in Fig. 2.2. Here, $\rho(\mu\text{m})$ is the radial distance away from the center of the VCSEL. For simplicity, the weakly guiding approximation is used that results in linearly polarized (LP) modes.

The fundamental mode (LP_{01}) is seen to take on the form similar to a Gaussian centered in the device. However, the higher-order modes (LP_{11}, LP_{21}, and LP_{02}), are spread spatially near the edge of the oxide-aperture that corresponds to the outer dielectric layer. This spatial discrimination of optical modes is the basis for many mode-control methods. Some methods, such as the surface-relief method [25, 28], intentionally damage or passivate regions of the DBR that primarily overlap with HOM. This raises the threshold modal gain for HOMs while leaving the fundamnetal mode unaffected to achieve single-mode operation. Other methods employ anti-guiding techniques such as photonic crystals [29], high-contrast gratings [30], and anti-resonant reflecting optical waveguide (ARROW) designs [31] achieve single-mode operation by either disrupting the resonance condition or index-guiding of HOM through the placement of a low-index material or phase-shifted layer. However, several of these methods require expensive regrowth steps or complex fabrication processes that limit its scalability for high-volume manufacturing.

Impurity-induced disordering is a mode-control method that raises the threshold modal gain of HOM compared to the fundamental mode. Disordering intermixes the discrete DBR pairs thus effectively reducing the optical mirror reflectivity in the disordered regions. In addition, when IID is initiated via Zn-diffusion, the high concentration of doping also increases the absorption losses in this regions. The overall effect is a greatly increased threshold modal gain for overlapping HOM. One of the main benefits that separates impurity-induced disordering from other methods is that it is commonly formed through the process of diffusion. Since the early stages of semiconductor fabrication, atomic diffusion has played a critical role in wafer-scale manufacturing [16]. The capability to introduce a foreign species in a controllable, non-destructive, and low-cost manner has made diffusion processes a core fabrication process.

2.3 Impurity-Induced Disordering

Impurity-induced disordering (IID) was discovered by Laidig and Holonyak at the University of Illinois at Urbana-Champaign (UIUC) in 1981 [32]. They recognized that diffusing Zn into a discrete AlAs/GaAs superlattice would promote intermixing across the sub-lattice boundaries. This caused discrete

superlattice pairs to disorder and form a homogenous, indirect bandgap $Al_xGa_{1-x}As$ material with an averaged aluminum content [32, 33] of the original superlattice. To illustrate this effect, an angle lapped optical micrograph of a disordered superlattice is shown in Fig. 2.3.

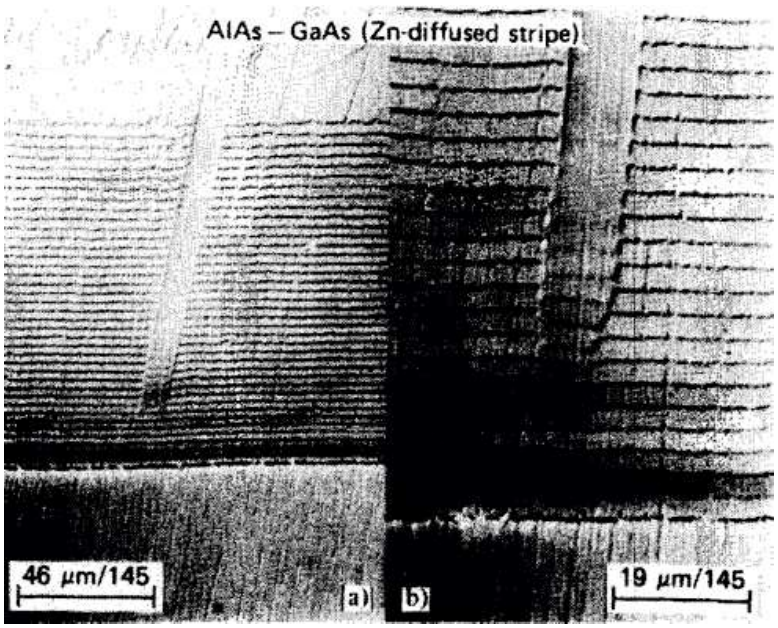

Figure 2.3: Angle lapped optical micrograph of a Zn-diffused stripe in an AlAs-GaAs superlattice from [32].

It is clear that the discrete superlattice pairs become disordered as a result of Zn diffusion. This mechanism is attributed to the greatly increased self-diffusion rates of the group III (Al and Ga) atoms in the crystal and across the sub-lattice boundaries. However, the self-diffusion rate is greatly dependent on the arsenic overpressure and concentration of native defects in the crystal, since these create pathways that the group III atoms can propagate through [33]. In the absence of Zn, the concentration of native defects in GaAs crystals is fairly low compared to the concentration of group III atoms ($\approx 2 \times 10^{22}$ cm^{-3}). Thus, intermixing is not generally observed at temperatures lower than the dissociation limit. Consequently, disordering processes can occur due to a defect that is created due to a requisite effect taken place such as diffusion or ion implantation processes.

While many different impurities including both donors (Si, Ge, S, Sn, Se) and acceptors (Zn, Be, and Mg) were discovered to induce disordering [33], Zn carries a certain significance that will be discussed since it is the

most commonly used impurity in mode-controlled VCSELs. Zn diffused into GaAs material can occupy a substitutional site as a shallow acceptor (Zn_s^-) or on an interstitial site as a donor (Zn_i^+) on the Ga sublattice [33, 34]. The solubility of Zn_s is known to be much larger than that of Zn_i while the diffusivity of interstitials Zn_i greatly exceeds that of the substitutional Zn_s by several orders of magnitude. The mechanism of Zn interstitial and substitutional diffusion was first explained by Longini [35] involving a gallium vacancy mechanism:

$$Zn_i^+ + V_{Ga} \rightleftharpoons Zn_s^i + 2h^+ \text{ [35]} \tag{2.1}$$

Shown in Eqn. 2.1, the holes (h^+) were widely believed to be dependent on the concentration of substitutional Zn_s^- [35]. However, Gösele and Morehead proposed that the "kick-out" mechanism was a more accurate model for the diffusion of Zn in GaAs [34].

$$Zn_i^+ \rightleftharpoons Zn_s^i + I_{Ga} + 2h^+ \text{ [34]} \tag{2.2}$$

Equation 2.2 describes the mechanism in which Zn_i^+ diffuses quickly through the crystal and dislodges group III (Ga) atoms. This results in the generation of Frenkel pairs (group III vacancies) in the lattice:

$$V_{Ga} + I_{Ga} \rightleftharpoons Ga_{Ga} \text{ [34]} \tag{2.3}$$

This finding is significant in explaining the physical mechanisms of disordering in AlAs/GaAs-based superlattices. In essence, diffused Zn via the "kick-out" mechanism, creates a large concentration of group III (Ga or Al) vacancies. This process is illustrated with corresponding figures for clarity and were modified from [27]. Fig. 2.4 shows Zn (red) diffusing into an AlAs-GaAs superlattice where Ga (navy), Al (cyan), As (gray), and atomic vacancies (white) are shown in a 2-D Zinc-Blende lattice structure. During the diffusion process, through the "kick-out" mechanism, interstitial Zn atoms can dislodge group III (Ga or Al) atoms and create corresponding vacancies that are together known as Frenkel pairs.

Figure 2.5 shows the interstitial diffusing Zn kicking out group III atoms from their lattice sites and generating Frenkel pairs. At this point, the Zn can either take the group III vacancy, thereby becoming a substitutional diffuser

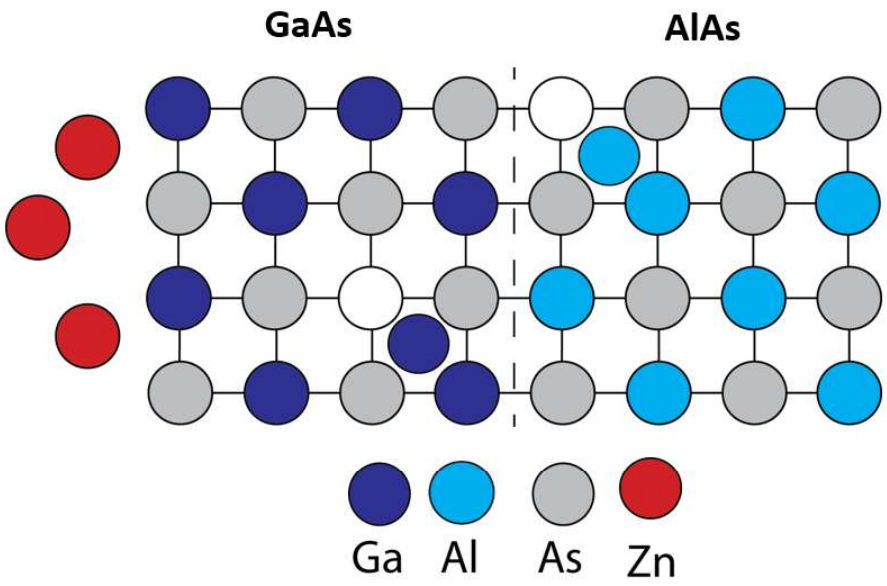

Figure 2.4: Illustration of Zn diffusing into an AlAs-GaAs superlattice.

and act as a shallow acceptor, or continue to propagate down the crystal shown in Fig. 2.6.

The interstitial group III (Al and Ga) atoms are then free to proceed across the sub-lattice that is promoted by annealing and complete the intermixing process as shown in Fig. 2.7. From the step-by-step analysis of impurity-induced disordering, there are several key effects that are advantageous for single-mode VCSELs. The first, is that it is initiated by the diffusion of Zn into an AlAs-GaAs based system which is directly compatible with $Al_xGa_{1-x}As$ based VCSELs. Secondly, intermixing causes discrete superlattice pairs to become smeared into a homogenous bulk $Al_xGa_{1-x}As$. This leads to a controllable method of lowering the mirror reflectivity of certain modes distinguished by their spatial mode profile. Lastly, it provides a large concentration of additional p-type doping to the superlattice which can be used to reduce series contact resistance for lower thresholds and higher wall-plug efficiencies.

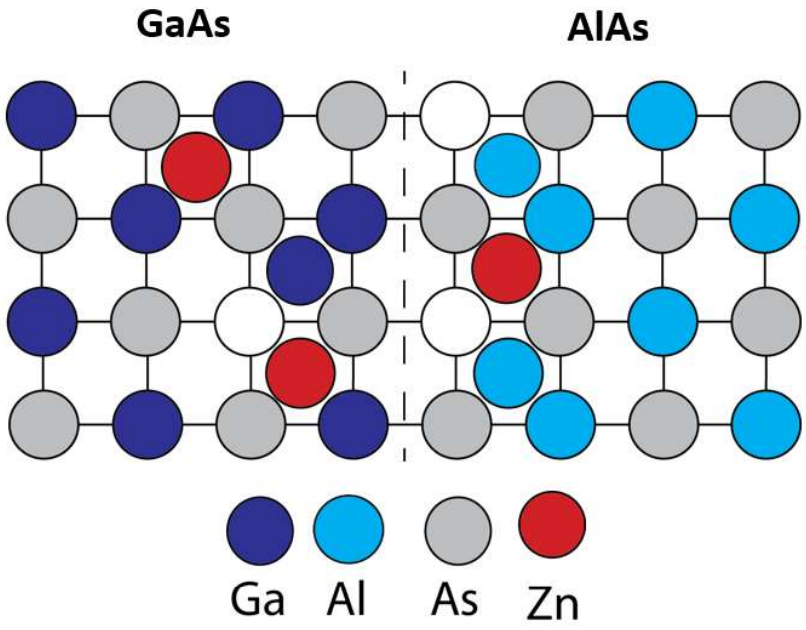

Figure 2.5: "Kick-Out" mechanism of interstitial diffusing Zn.

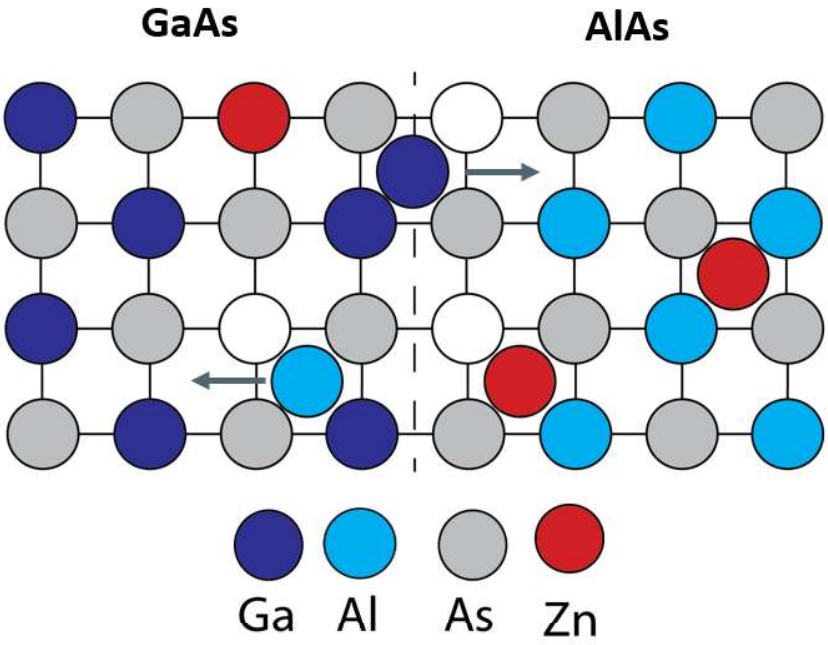

Figure 2.6: Zn either substitutionally fills the vacancy or propagate down the crystal.

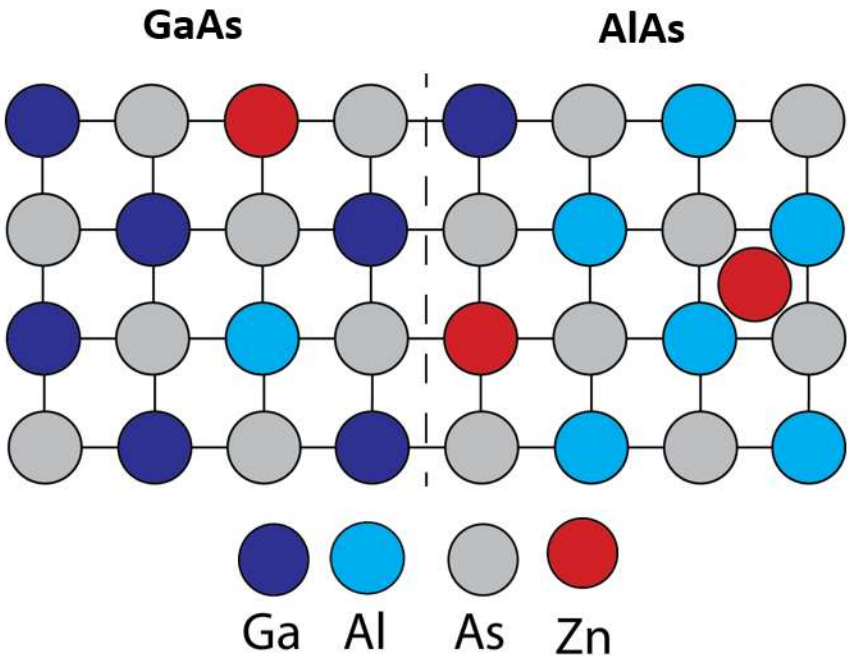

Figure 2.7: Group III (Al and Ga) atoms self-diffuse across the sub-lattice boundary and fulfill the intermixing process.

CHAPTER 3

DESIGN AND FABRICATION OF IMPURITY-INDUCED DISORDERD VCSELS

3.1 Design of Impurity-Induced Disordering Aperture

As discussed in the Section 2.3, impurity-induced disordering via diffusion of Zn into an $Al_xGa_{1-x}As$ based superlattice result in unique effects for optical mode control in VCSELs. Most significantly, the intermixed regions of the $Al_xGa_{1-x}As$-based Bragg reflector (DBR) will have higher mirror losses than in the non-disordered regions. Due to the spatial discrimination of the supported optical modes in a VCSEL, disordering formed in the shape of an aperture can lead to an increased threshold modal gain for HOM while relatively unaffecting the fundamental-mode, thus achieving single-mode performance. In addition, when disordering is induced on the p-DBR of the VCSEL, the additional p-type doping can lead to increased free-carrier absorption, lower series resistance, and increased wall-plug efficiency. Therefore, optical modes overlapping the disordering aperture will not only experience lower optical mirror loss but also higher absorption losses. This leads to significant increases in the threshold modal gain for the affected modes.

The optical mirror loss induced by disordering can be modeled by the transfer-matrix method (TMM). The transfer-matrix method is a commonly used method of calculating the incident, reflected, and transmitted electric-field through each layer in a matrix form. Since VCSELs are composed of many DBR and supplementary layers, matrix calculations greatly facilitates computational time and complexity of these structures. Here, we will invoke the formulation of the backward propagation transfer matrix method derived from [36].

A computational model of a disordered DBR structure used for this calculation is shown in Fig. 3.1. The non-disordered DBR structure consists of alternating $Al_{0.15}Ga_{0.85}As/Al_{0.90}Ga_{0.10}As$ that are both quarter-wavelength

thick. The thicknesses used for this calculation are 60.25 and 69.53 nm for $Al_{0.15}Ga_{0.85}As$ and $Al_{0.90}Ga_{0.10}As$ respectively. In this calculation, it is also noted DBR structure consists of 20 total pairs. Since the disordering effect intermixes the discrete DBR pairs into homogenous bulk $Al_xGa_{1-x}As$ layers with an averaged aluminum composition [32, 33], the disordered layers are modeled as completely disordered $Al_{0.525}Ga_{0.475}As$.

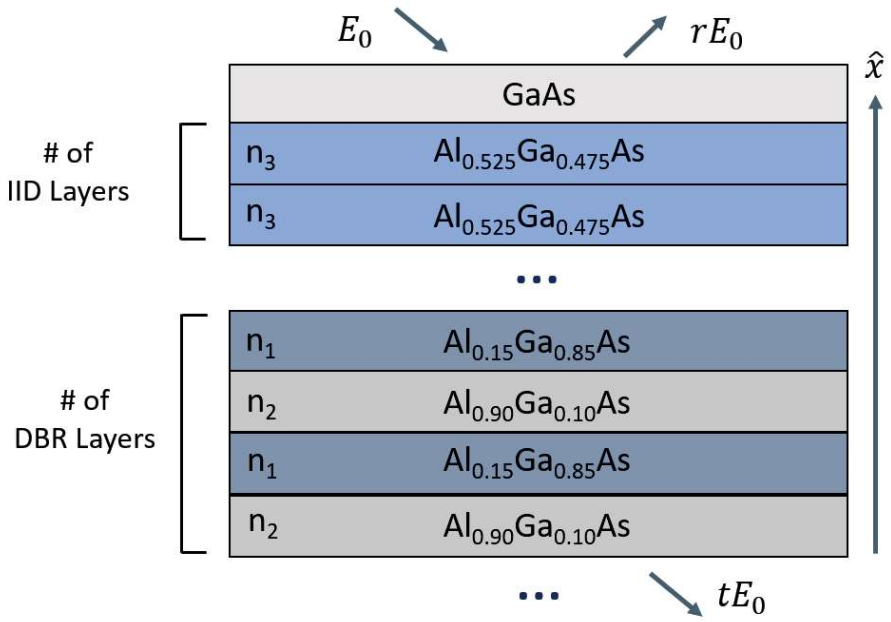

Figure 3.1: Model of an impurity-induced disordered DBR structure.

For a transverse-electric (TE) polarized wave, the incident and reflected field given in a layer can be defined as [36]

$$E_i = \hat{y}E_0 e^{-ik_{0x}x + ik_{0z}z} \tag{3.1}$$

$$E_r = \hat{y}rE_0 e^{+ik_{0x}x + ik_{0z}z} \tag{3.2}$$

Thus, in the lth layer, the total electric-field can be found by the superposition of the incident and reflected fields through the following:

$$E_l^y = [A_l e^{-ik_{lx}(x+d_l)} + B_l e^{ik_{lx}(x+d_l)}]e^{ik_{lz}z} \tag{3.3}$$

The corresponding magnetic-fields for these layers can also be given by:

$$H_z = \frac{1}{iwu_l}\frac{\partial}{\partial_x}E_y \tag{3.4}$$

At the interface of each layer, the boundary conditions that must be satisfied require a continuous E_y and H_z across the interface of two different media. This leads to the following relation:

$$\begin{bmatrix} A_l \\ B_l \end{bmatrix} = \mathbf{B}_{l(l+1)} \begin{bmatrix} A_{1+1} \\ B_{1+1} \end{bmatrix} \tag{3.5}$$

The backward-propagation matrix $\mathbf{B}_{l(l+1)}$ that links the electric-fields of two interfacing layers can be defined as:

$$\mathbf{B}_{1(l+1)} = \frac{1}{2}\begin{bmatrix} (1+P_{l(l+1)})e^{-ik_{l+1}h_{(l+1)x}} & (1-P_{l(l+1)})e^{ik_{l+1}h_{(l+1)x}} \\ (1-P_{l(l+1)})e^{-ik_{l+1}h_{(l+1)x}} & (1+P_{l(l+1)})e^{ik_{l+1}h_{(l+1)x}} \end{bmatrix} \tag{3.6}$$

where $P_{l(l+1)}$ is defined as:

$$P_{1(l+1)} = \frac{\mu_l k_{(l+1)x}}{\mu_{l+1} k_{lx}} \tag{3.7}$$

and the thickness of region l is defined as:

$$h_{l+1} = d_{l+1} - d_l \tag{3.8}$$

Immediately, it is clear that for an $Al_xGa_{1-x}As$-based DBR, $P_{1(l+1)}$ collapses to merely the ratios of the index of refraction of interfacing layers in a system of non-magnetic material. The experimentally measured index of refractions of $Al_xGa_{1-x}As$ for a given design wavelength of $\lambda = 850$ nm is referenced in the TMM calculation [37]. The calculation of the electric field components

$Al_{0.15}Ga_{0.85}As$ (n_1)	$Al_{0.90}Ga_{0.10}As$ (n_2)	$Al_{0.525}Ga_{0.475}As$ (n_3)
3.5269	3.0561	3.3925

Figure 3.2: Index of refractions calculated for various $Al_xGa_{1-x}As$ used in TMM calculation.

incident (E_0), reflected (rE_0), and transmitted (tE_0) through the total DBR layer as depicted in Fig. 3.1 can be simplified by the following:

$$\begin{bmatrix} E_0 \\ rE_0 \end{bmatrix} = (\mathbf{B}_{\mathrm{GaAs}})(\mathbf{B}_{\mathrm{IID1}}\mathbf{B}_{\mathrm{IID2}})^{\#\mathrm{IID}}(\mathbf{B}_{\mathrm{DBR1}}\mathbf{B}_{\mathrm{DBR2}})^{\#\mathrm{DBR}} \begin{bmatrix} tE_0 \\ 0 \end{bmatrix} \tag{3.9}$$

The backward propagation matrix can then be further condensed into a single backward-propagation matrix resulting in the following notation:

$$\begin{bmatrix} E_0 \\ rE_0 \end{bmatrix} = \begin{bmatrix} b_{11} & b_{12} \\ b_{21} & b_{22} \end{bmatrix} \begin{bmatrix} tE_0 \\ 0 \end{bmatrix} \tag{3.10}$$

and thus the electric-field transmission (t)

$$t = \frac{1}{b_{11}} \tag{3.11}$$

and reflection (r) coefficients can be calculated.

$$r = \frac{b_{21}}{b_{11}} \tag{3.12}$$

Employing the backward TMM derived with the index of refraction values in Fig. 3.2, the optical power reflectivity for varying degrees of disordering is shown in Fig. 3.3. As shown, the non-disordered DBR functions as a highly reflective optical mirror, achieving a peak optical power reflectivity of 98.99%. With the diffusion of Zn into the top DBR, it is evident that the optical power reflectivity and stopband width begins to decrease with increased amounts of disordering. For 3, 5 and 7 IID pairs, the peak optical power reflectivity decreases to 97.55%, 95.64%, and 92.25% respectively.

When the threshold modal gain in a VCSEL is examined, the utilization of impurity-induced disordering for higher-order mode suppression becomes clear. In Fig. 3.4, an illustration showing a VCSEL structure where the optical cavity is terminated by a pair of DBR on either side. During the injection of current into a laser, the lasing threshold is met when the total optical gain equalizes the total mirror and intrinsic losses in a device. The gain in a VCSEL is supplied injected electrons populating the upper-state of the quantum-well region. The threshold modal gain equation can be derived

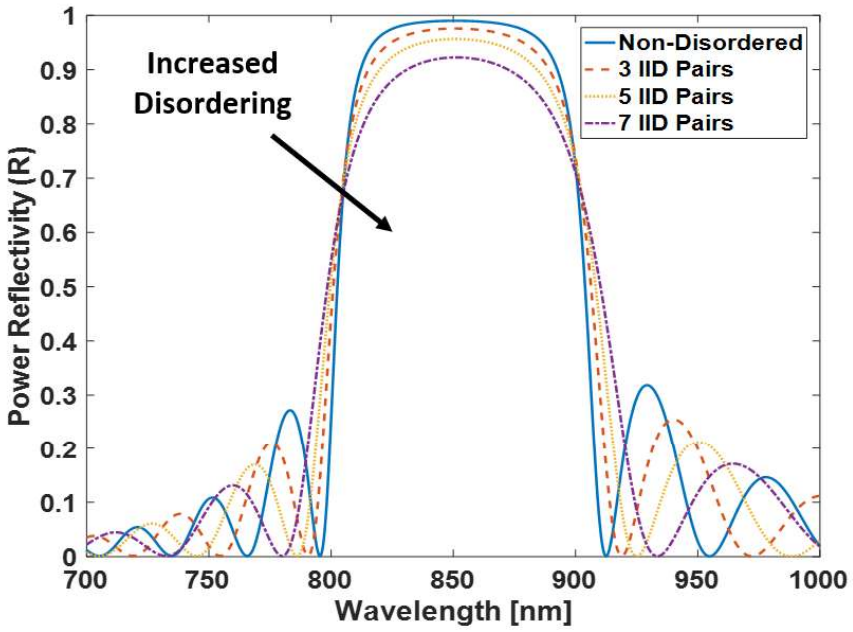

Figure 3.3: Calculation of optical power reflectivity ($R = |r|^2$) for varying degrees of disordering [16].

by requiring the round-trip gain to be unity and phase-matched [36]. Due to a small cavity length in addition to the highly reflective optical mirrors (R_1, R_2) on both sides, the intrinsic and mirror losses (α) in a VCSEL are overcome from the gain supplied at small current-injection levels and thus exhibit low thresholds.

$$\Gamma g_{th} = \alpha - \frac{1}{2L}\ln(R_1 R2) \tag{3.13}$$

However, when the power reflectivity decreases as a result of impurity-induced disordering, optical modes that overlap the disordering region will experience an increased threshold modal gain. Consequently, optical modes that are not affected by the disordering region can begin lasing and consuming the gain available more readily than higher-order modes. This is the principle of higher-order mode suppression and has been demonstrated to achieve single-mode operation and emit at high (milliwatt) level powers [17].

As shown in Fig. 3.5, an impurity-induced disordered (IID) VCSEL structure takes the form of an oxide-confined VCSEL structure with a disordering aperture formed via selective Zn diffusion in the top DBR [16, 17]. The Zn causes the diffused DBR to intermix and form smooth homogenous

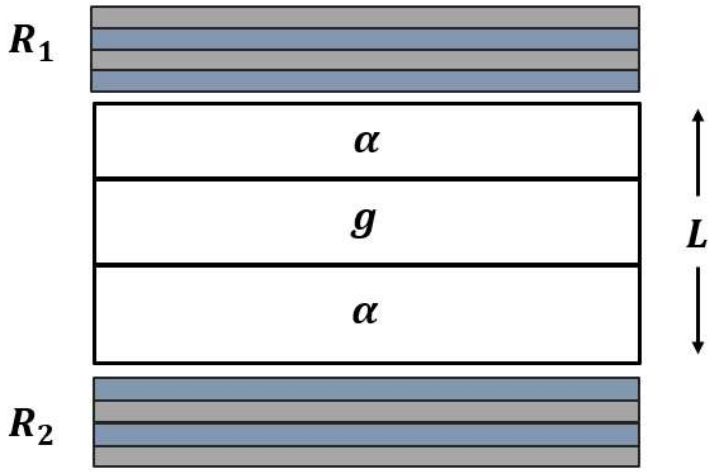

Figure 3.4: Illustration of a VCSEL cavity for threshold modal gain analysis.

$Al_xGa_{1-x}As$ material that increases the threshold modal gain for the optical modes impinged on the disordered region due to increased mirror losses. A scanning electron microscopy (SEM) image is shown where the diffusion of Zn is visually emphasized through the process of stain etching [38, 39].

To demonstrate this effect, oxide-confined VCSELs with an oxide aperture of 3.0 μm are fabricated. The oxide aperture size is designed to allow several higher-order modes to lase without any modifications to the device. Impurity-induced disordering apertures are then formed to primarily overlap with the higher-order modes while leaving the center, where the fundamental mode lies, relatively unaffected. The characterization of these devices has been published in other works [16, 17, 27], however, the findings of this work motivate the necessity for a method of controlling the impurity-induced disordering apertures for finer mode-control that can enable improved performance. Thus, several key points of the characterized devices will be shown and discussed.

3.2 Fabrication of Impurity-Induced Disordered VCSEL

The epitaxial structure employed for this work consists of an n-doped GaAs substrate that was grown via metal-organic chemical vapor deposition (MOCVD)

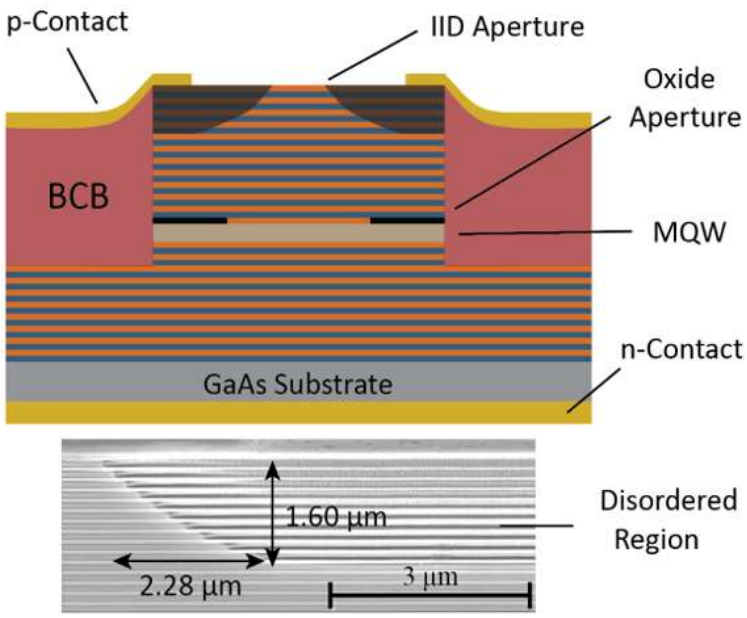

Figure 3.5: Schematic of an impurity-induced disordered VCSEL [16].

by EpiWorks in Champaign, Illinois. The epitaxial structure first begins by the growth of 37 pairs of n-type $Al_{0.90}Ga_{0.10}As/Al_{0.15}Ga_{0.85}As$ pairs. The active region consists of three GaAs quantum-wells surrounded by $Al_{0.3}Ga_{0.7}As$ barrier layers. Thicker $Al_{0.3}Ga_{0.7}As$ layers are additionally placed on both sides of the active region to serve as cladding layers for improved optical confinement. Then a single high-aluminum ($Al_{0.99}Ga_{0.01}As$) layer for oxide-aperture formation during processing is grown after the active region. Finally, the top DBR, consisting of 20 pairs of p-type $Al_{0.90}Ga_{0.10}As/Al_{0.15}Ga_{0.85}As$, is grown with a highly conductive p-type GaAs cap that terminates the epitaxial structure. The highly conductive p-type GaAs layer is used to enhance current spreading into the top of the device [17, 40]. Both the n- and p-type DBRs contain grading layers between the $Al_{0.90}Ga_{0.10}As/Al_{0.15}Ga_{0.85}As$ interface to reduce the series resistance of the DBR layers.

The fabrication process of the IID VCSELs presented in this work begins with the GaAs cap being etched down to a thickness of 100 nm. Other work based on this epitaxial structure has shown reduced phase-related mirror loss when the GaAs cap layer is etched down from 140 nm to 100 nm [16, 17, 40]. Following the cap etch, the disordering process is carried out through a sealed ampoule diffusion process. First, the epitaxial samples are patterned with an STS Plasma Enhanced Chemical Vapor Deposition (PECVD) system that is

equipped with the capability of in-situ switching between a high-frequency (13.56 MHz) and low-frequency (380 kHz) plasma source during deposition. Approximately 50 nm of high-frequency sourced SiN_x is deposited onto the sample. They are then photolithographically patterned with circular pillars. The pillar diameters define the IID aperture size that is formed during Zn diffusion. The photolithographic pattern is then transferred into the SiN_x diffusion mask through reactive-ion etching (RIE) using a PlasmaLab RIE supplied with CF_4/O_2 gasses.

Figure 3.6: Vacuum sealed quartz tube with crystalline $ZnAs_2$ source and VCSEL sample separated by glass barrier.

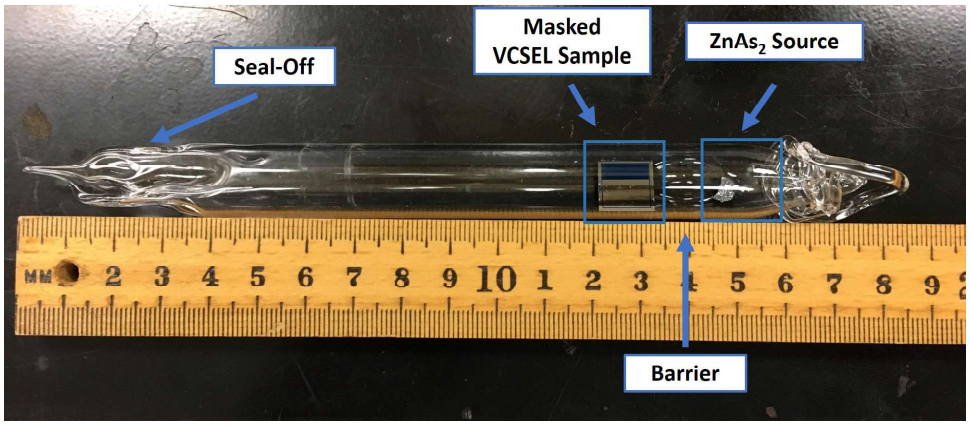

Figure 3.7: Annotations to supplement Fig. 3.6 for clarity.

Quartz tubes are prepared for ampoule seal-offs by immersing the interior and exterior of the tube in dilute buffered oxide etchant (BOE) for 2.5 to 3 hours. This facilitates the removal of any particulates and contaminants.

Prior to cleaning, one end of the quartz tube is sealed off where a hook is made in order to attach a push rod at the end to maneuver the tube in the diffusion oven. Solid $ZnAs_2$ sources are weighed and loaded along with the patterned VCSEL sample into the quartz tube. Prior to loading, a glass barrier is formed near the end of the tube to ensure the epitaxial sample and diffusion source remain separated during the process of diffusion. Then, the tube is inserted onto the diffusion pump based vacuum system to reach vacuum pressures (< 5 x 10^{-6} Torr). The open end of the quartz tube is then sealed to form an ampoule. Figure 3.6 shows a patterned VCSEL epitaxial sample sealed under vacuum with a solid $ZnAs_2$ source separated by the glass barrier as discussed. Figure 3.7 provides an annotated image of Fig. 3.6 for clarity. The ampoule is then loaded into a dry furnace set at 600° C for 80 minutes. This initiates the formation of IID apertures into the top p-DBR of the VCSEL sample. While this work demonstrates the initiation of disordering by method of ampoule seal-offs, more scalable methods of Zn-diffusion has been demonstrated by [41, 42].

Once the disordering process is complete, the SiN_x diffusion mask is removed and the VCSEL epitaxial samples undergo a traditional oxide-confined VCSEL fabrication process. A separate SiN_x film is deposited using an STS PECVD to serve as a hard mask during the mesa etch process. The SiN_x is lithographically patterned and transferred similarly to the SiN_x diffusion mask. Utilizing an Oxford PlasmaLab System 100 Inductive Coupled Plasma - Reactive Ion Etching (ICP - RIE) system, VCSEL mesas are defined through careful balancing of $BCl_3/H_2/Ar$ gasses. Anistropic etching and minimal sidewall roughness is desirable for optimal electro-optical performance.

As shown in Fig. 3.8, smooth anisotropic sidewalls are achieved using a combination of $BCl_3/H_2/Ar$ gasses and RIE/ICP power. An enlarged view of the sidewall is also shown in Fig. 3.9. It is noted that other gas combinations including BCl_3/Cl_2 also demonstrated good sidewall and etching performance during the development of this work. The VCSEL mesa etch depth is monitored through an in-situ laser interferometry system where the number of etched pairs can be closely monitored. The mesa etch is stopped after the etch begins to reach 1-2 pairs of the bottom n-DBR which results in an approximate etch depth of 3.5 - 3.6 μm of material. In addition to device isolation, the mesa etch is designed to expose the high-aluminum con-

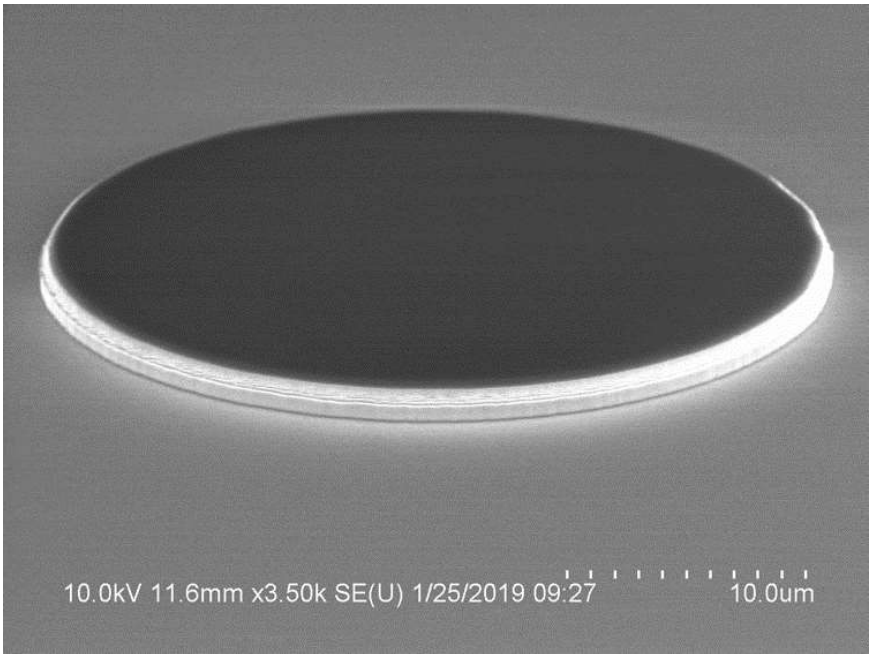

Figure 3.8: Calibration etch of bulk GaAs with intact SiN_x dielectric mask to achieve anisotropic etching and minimal sidewall roughness.

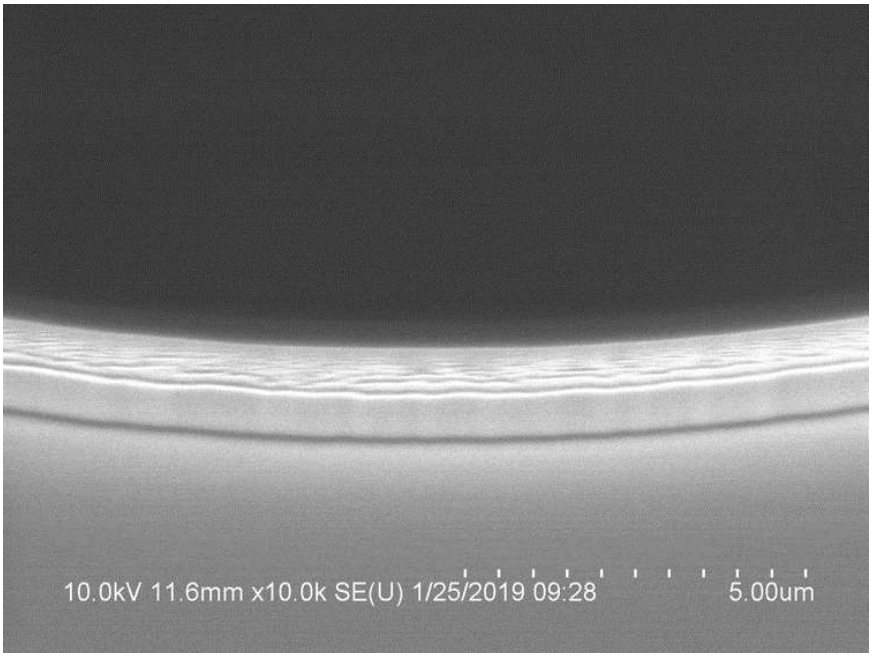

Figure 3.9: Enlarged view of GaAs etch sidewall.

tent layer. An oxide-aperture is formed through exposing the etched VCSEL samples in a wet oxidation furnace where vaporous H_2O/N_2 is flowed into the oven chamber. It is noted that other exposed high-aluminum content layers will begin to oxidize as well, however, the oxidation rate greatly depends on the aluminum composition and thickness of the layer [4, 23]. The devices are then planarized using a spin-on polymer, benzocycobutene (BCB) and thermally cured under vacuum at 250 °C for 2 hours. An etch-back process using a PlasmaLab RIE system with CF_4/O_2 gasses is then performed to fully remove any polymer on the VCSEL mesas for p-contacts and form vias for n-contacts if desired. The top p-electrode layer (Ti/Pt/Au) is deposited via standard electron-beam evaporation and lithographic lift-off procedures. For backside contact formation, the n-type substrate is thinned via mechanical lapping and chemical polishing process. Lapping slurries, consisting of alumina oxide powder and de-ionized water, are used to thin the substrate down to approximately 100 μm in thickness. The grit size of the alumina oxide powder is slowly graded during the process to form a smooth back-side surface finish. Then, a chemical polishing step using dilute sodium hypchlorite (NaOCl) is used to polish until a mirror-like finish is achieved. The back-side n-contact (AuGe/Ni/Au) is then deposited and annealed at 405°C to form a low-resistance ohmic contact. This concludes the fabrication of the impurity-induced disordering presented in this work.

A focused ion beam scanning electron microscope (FIB-SEM) image showing the cross-sectioning of an IID VCSEL is shown in Fig. 3.10. Prior to ion milling, a protective layer of Pt is sputtered on the top surface that is shown in the image. This protective layer is not present during normal operation.

3.3 Device Characterization of IID VCSELs

The light-current-voltage (LIV) characteristics and modal behavior of various IID aperture sizes have been discussed elsewhere [16, 17, 27]. The IID VCSELs presented were fabricated with an oxide-aperture of approximately 3.0 μm across all devices. The IID aperture size, however, is varied between 0.4 μm to 1.9 μm. It is noted that the IID aperture size is designed to be smaller than the oxide-aperture. By doing so, the IID aperture behaves as a filter for the optical modes supported by the oxide-aperture. This empha-

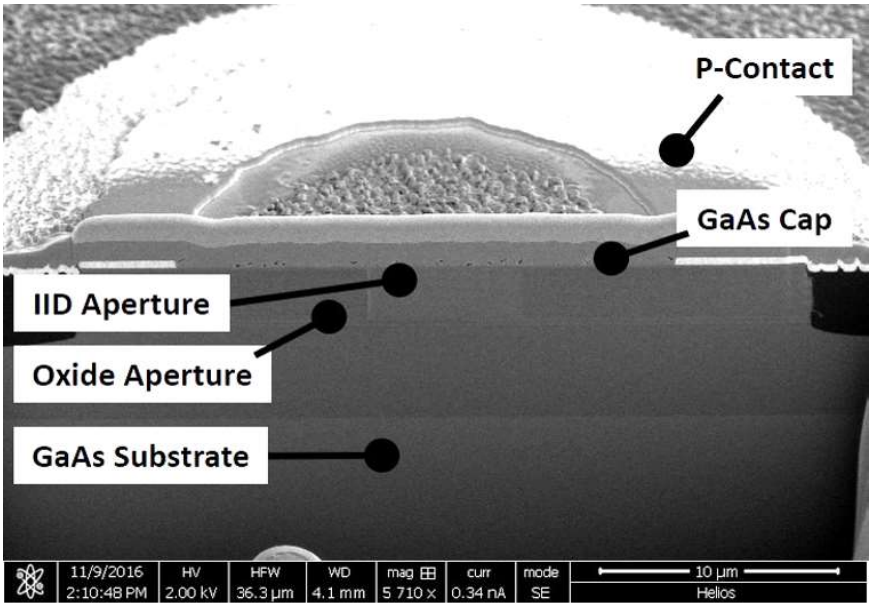

Figure 3.10: FIB-SEM Cross-sectioning for fabrication verification of IID VCSEL [16].

sizes the mode-suppression effects of the IID aperture and can be used to observe the mode suppression limitations of the IID apertures formed. From Fig. 3.5, the IID aperture depth is determined to be approximately 2.28 μm for a disordering time of 80 minutes at 600 °C.

As shown in Fig. 3.11, the light-current-voltage (LIV) and optical spectra measurements for IID aperture sizes ranging from 1.0 μm to 1.6 μm are measured [17, 27]. It is noted that the series resistance for the disordered devices reduced from 146 Ω to 68 Ω as a result of enhanced current spreading and additional p-doping in the GaAs conductive cap layer. Beginning with the smallest IID aperture size, the device operates at single-fundamental-mode throughout the entire current sweep of the measurement. In this work, single-mode performance is defined by a side-mode suppression ratio (SMSR) greater than 30 dB. This device, however, suffered from immense self-heating effects that led to lowest output power emission among all of the IID aperture sizes. As the IID aperture size is increased to 1.0 μm, the device still maintains single-mode operation throughout the entire current sweep of the measurement exhibiting an SMSR of approximately 35 dB. The threshold current is measured to be 332 μA where the maximum fundamental mode output power collected is measured to be 1.26 mW. As the IID aperture size is further increased to 1.3 μm, the threshold begins to decrease to 271 μm

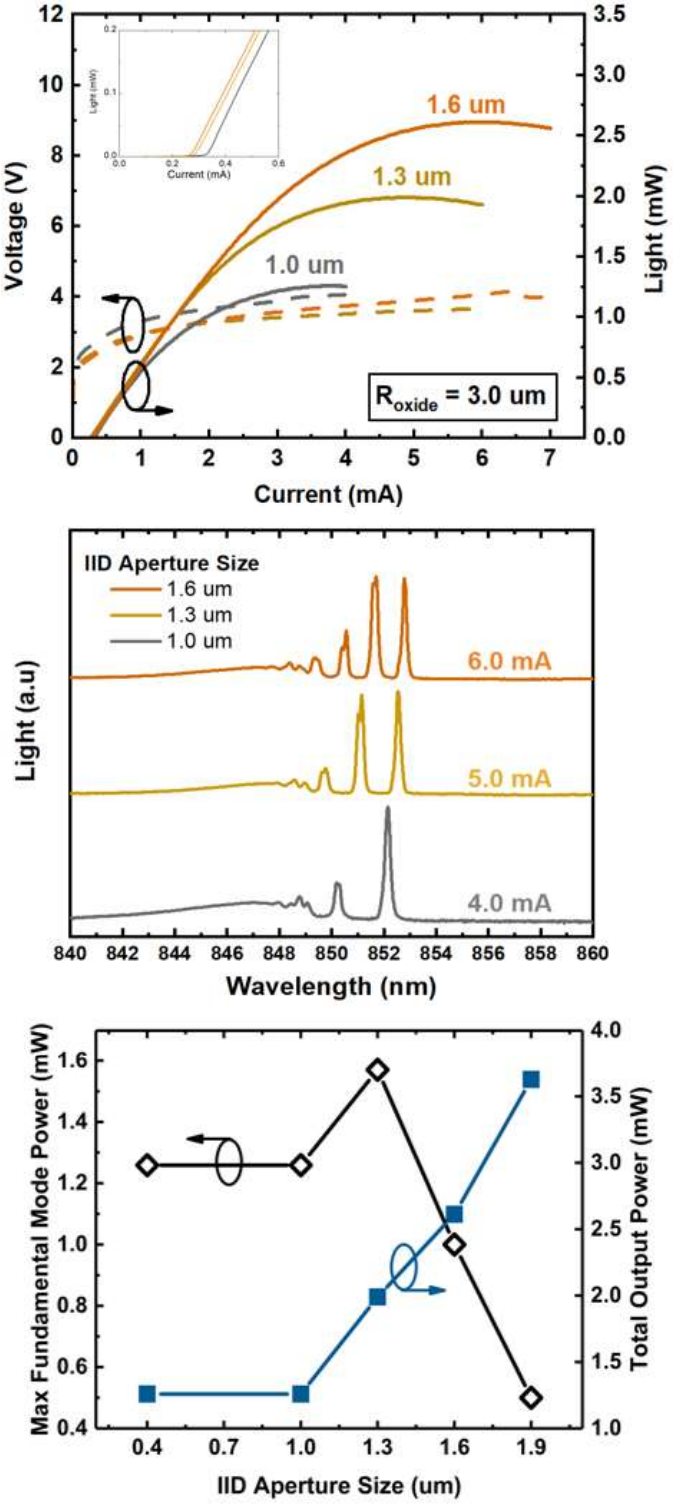

Figure 3.11: Light-current-voltage (LIV) measurements for various sized IID apertures (top). Optical spectra for various IID aperture sizes and injection current levels (middle). Maximum fundamental mode power and total output power for various IID aperture sizes (bottom). Figures are adapted from [17].

while the maximum fundamental mode power collected also increases to 1.6 mW. It is noted that for lower current injection levels ($<$ 4 mA), this device maintains single-fundamental-mode operation, but begins to operate in few-mode operation at larger current injection levels. As the IID aperture size further increases to 1.6 μm, the current threshold begins to increase to 300 μm and the emission begins to operate at multi-mode operation during the entire current sweep of the measurement. While the total output power, as shown in Fig. 3.11, begins to increase, the maximum fundamental mode power recorded for this device greatly decreases since it is mainly emitting in multi-mode operation.

To facilitate the discussion of the IID aperture overlap with the fundamental mode versus the higher-order modes, the various sized disordering apertures (gray shading) are illustrated to overlap the fundamental and higher-order mode electric-field profile for various IID aperture sizes in Fig. 3.12. It can be seen that for small IID aperture sizes (0.4 and 1.0 μm), the disordering region, which acts as an absorber, generates a significant amount of self-heating that causes thermal rollover to occur quite rapidly. While the HOM suppression is sufficient to achieve single-mode operation, the disordering aperture size may be encroaching the fundamental mode and thus limited output power is achieved in these devices. As the IID aperture is further increased to 1.3 μm, the optimal IID aperture size for high-power single-mode operation is achieved with a maximum fundamental mode power of 1.6 mW. The amount of HOM suppression by disordering is sufficient enough while not inducing significant free-carrier absorption and self-heating that would otherwise limit the output power of the device. Therefore, an optimal 1.3 μm IID aperture for these devices is experimentally demonstrated. As the IID aperture is then increased to the largest sizes (1.6 and 1.9 μm), the total output power becomes the greatest as shown at the bottom of Fig. 3.11, however, the device operates almost entirely in the multi-mode regime. This is because the disordering aperture is insufficient in higher-order mode suppression and does not significantly overlap the HOM as depicted in Fig. 3.12.

From the modal analysis presented of various IID aperture sized VCSELs, disordering provides a wafer-scale method of modifying multi-mode VCSELs to single-mode operation. This is achieved through disordering the top p-DBR in the shape of an aperture that induces significant mirror loss to regions

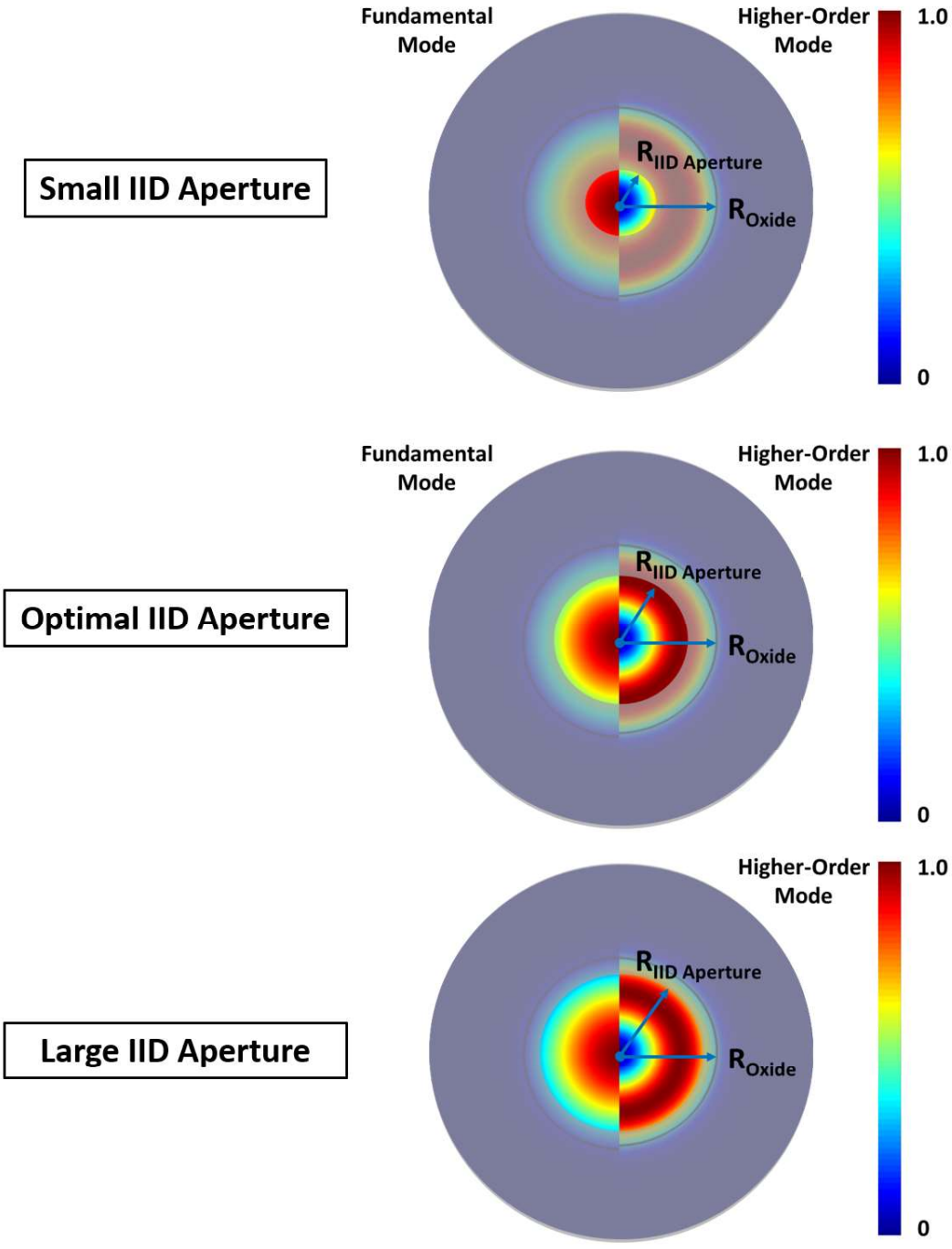

Figure 3.12: Transverse optical mode profiles for various IID aperture sizes.

that overlap primarily HOM. This method also increases p-type doping which reduces series resistance and enhances current spreading at the p-contact. The advantageous properties of disordering, however, can be overshadowed by adverse effects by encroaching onto the fundamental-mode. This leads to significant self-heating which limits the output power emitted and thereby performance of the device.

For optical mode control, it is thus desirable to induce deep disordering apertures while maintaining a designed IID aperture size. Since the shape of the disordering aperture is governed by diffusion, there is an unavoidable portion of lateral diffusion that occurs. This can lead to unwanted diffusion underneath regions that are masked off, especially during deep disordering processes. The degree of lateral diffusion is defined by the curvature of the diffusion front. As shown in the modal behavior discussion, this encroachment can lead to reduced output powers due to increased self-heating if not properly mitigated. This motivates the development and demonstration of a capability to control the diffusion front curvature without sacrificing the manufacturability and scalability of the process. In Chapter 4, a method of controlling the IID aperture diffusion front by tailoring the strain of the diffusion mask is presented that enables the formation of more complex and fine-tuned IID aperture designs for high-power single-mode VCSELs.

CHAPTER 4

STRAIN-CONTROLLED IMPURITY-INDUCED DISORDERING APERTURES

4.1 Tailoring Diffusion Mask Strain

As discussed in the Section 3.3, a limitation of impurity-induced disordering lies in the isotropic nature of diffusion. During deep disordering processes, this can lead to undesirable lateral diffusion which can limit the enhancement effects for mode control, high-speed modulation, or high-power performance in VCSELs. This work demonstrates the capability to control the IID aperture profile through tailoring the diffusion mask strain used for disordering as outlined in Section 3.2.

The study of controlling strain in chemical-vapor-deposition (CVD) and plasma-enhanced-vapor-deposition (PECVD) grown SiN_x and SiO_2 thin films is widely reported in literature [16, 27, 43, 44, 45]. Both SiN_x and SiO_2 films are used as passivating dielectrics and thus numerous studies aimed to mitigate the film stress from these dielectrics were found to be critical for increased reliability and lifetimes of devices [43]. Separately, in an effort to mitigate the lateral diffusion of IID apertures formed when using high-frequency (13.56 MHz) deposited SiN_x diffusion masks, other frequency compositions of SiN_x, in addition to SiO2, were investigated for the use of diffusion masks. It was noted that the lateral-to-vertical (L/V) diffusion components would vary for differing frequency compositions of SiN_x. In this work, we define the compositions of the PECVD SiN_x deposited by their time compositions of high-frequency source depositions [16, 27]. Both low-frequency and high-frequency SiN_x can be deposited by the STS Multiplex PECVD, and additionally it can time periodically alternate between the two sources. As a result, a mixed-frequency film can be formed through time-alternating between the high- and low-frequency plasma source used for deposition. The composition of such a mixed-frequency film is illustrated in Fig. 4.1.

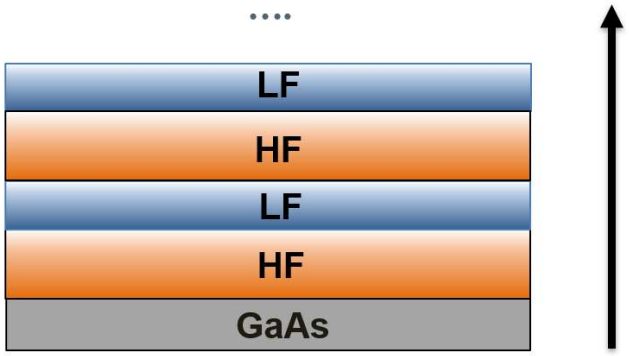

Figure 4.1: Illustration of mixed-frequency film deposition process.

Alternating layers of low-frequency (LF) and high-frequency (HF) sourced SiN_x are deposited until a total thickness of 50 nm is achieved. The high-frequency time-ratio is defined by Eqn. 4.1.

$$\text{HF Time Ratio} = \frac{\text{HF Deposition Time (s)}}{\text{HF Deposition Time (s)} + \text{LF Deposition Time (s)}} \tag{4.1}$$

In this work, the high-frequency film is deposited first. It is expected that the first interface between the sample and the dielectric thin film carries the largest influence. A variety of SiN_x were measured for their film stress characteristics. Utilizng an FSM 500 TC thin film stress measurement system, SiNx of various HF time ratio compositions were deposited and measured on various substrates. The film stress is calculated by invoking the Stoney equation [46]:

$$\text{Film Stress}(\sigma) = \frac{ED^2}{6(1-V)RT} \tag{4.2}$$

where E is the Young's modulus of the substrate, V is the Poisson's ratio of the substrate, D is the thickness of the substrate, and T is the thickness of the film where $T << D$ to satisfy the thin film approximation. R, which is measured via point-by-point subtraction data calculated before and after the deposition scan data of the measurement. This measurement effectively quantifies the bowing induced by the thin film. Due to the minute bowing that occurs, this system is only capable of accurately measuring substrate

sized samples. Due to the financial constraints of using epitaxial wafer substrates, a semi-insulating (SI) GaAs and intrinsic Si substrate wafer are used instead.

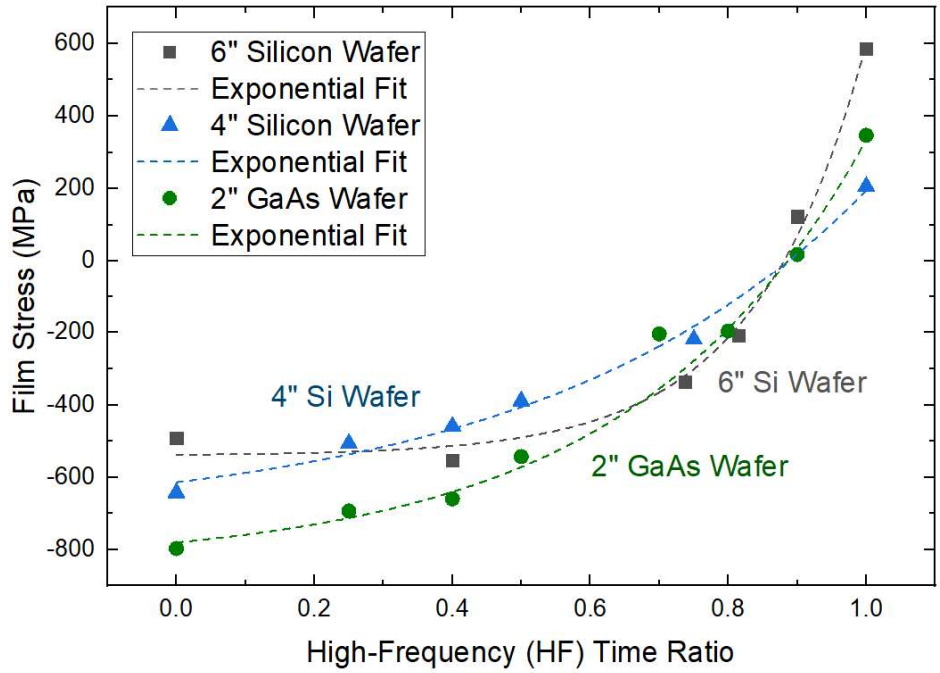

Figure 4.2: Film stress measurements of various SiN_x films on various substrates.

These measurements are shown in Fig. 4.2. It was found that the film stress as a function of high-frequency (HF) time ratio exhibited a monotonically increasing exponential-like behavior as a function of HF time ratio. It can be seen that GaAs and Si follow relatively similar trend lines. Since the VCSEL epitaxial samples are capped with a GaAs layer, the GaAs data is taken to represent the SiN_x film strain induced on the VCSEL samples during disordering. Film stresses between +347 MPa and -797 MPa are achieved through depositing various SiN_x thin film compositions on 2-inch GaAs wafers.

It is noted that the film strain induced by the diffusion masks employed for disordering must withstand high temperature ($> 500\ ^\circ$ C) anneals to initiate the disordering process. It was found that films with larger magnitude of strain (both tensile and compressive) showed degraded masks after being exposed to high-temperature conditions for several minutes as shown in Fig. 4.3. This led to fewer data points for IID apertures utilizing these films and

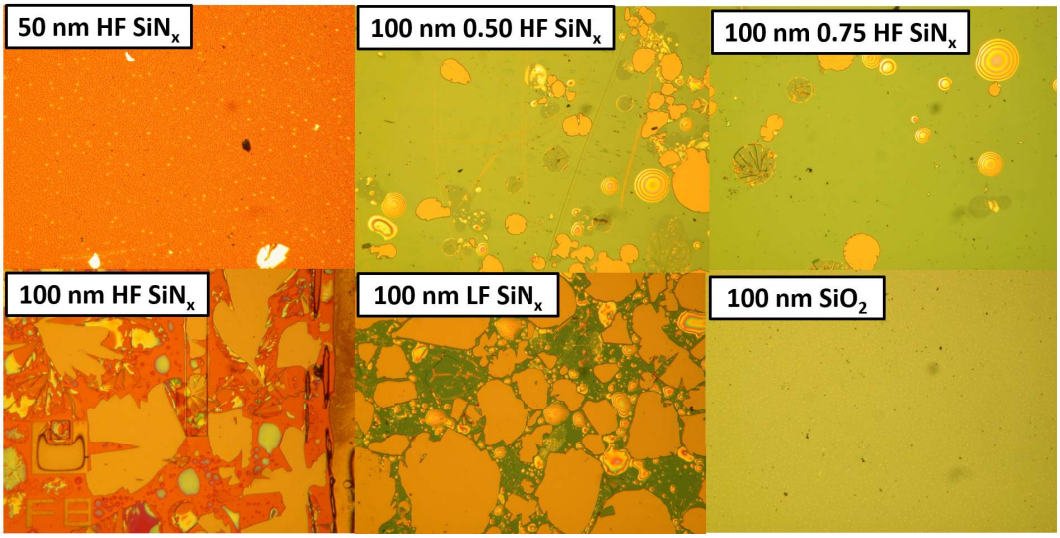

Figure 4.3: Diffusion mask conditions after 575° C for 15 minutes on InP substrates.

should be considered when designing a reliable method of controlling disordering apertures. It is noted that Fig. 4.3 shows dielectric films deposited on InP substrates that led to a slightly different degradation pattern compared to GaAs.

4.2 Modified IID Apertures via Mask Strain

The low-frequency, high-frequency, 0.70 and 0.90 HF time ratio films are then employed for IID aperture formation following the process outlined in Section 3.2. The diffusion masks are deposited and patterned into stripe vias in various widths from 10 to 20 μm along the sample. Therefore, various IID apertures were formed and measured for each diffusion mask composition deposited. The epitaxial samples are then cleaved and stained with K_3[[Fe(CN)$_6$]:KOH to highlight the diffusion profile. Prior to cleaving and staining, the epitaxial samples are protected with an additional SiN_x deposited layer. The samples are then inspected using a Hitachi S4800 scanning electron microscope (SEM).

As shown in Fig. 4.4, the IID apertures of the LF and HF sourced deposited SiN_x diffusion masks resulted in distinctly different diffusion fronts. These IID apertures are formed in n-type DBR calibration samples where the repeating $Al_{0.90}Ga_{0.10}As/Al_{0.15}Ga_{0.85}As$ pairs can be seen. In order to quan-

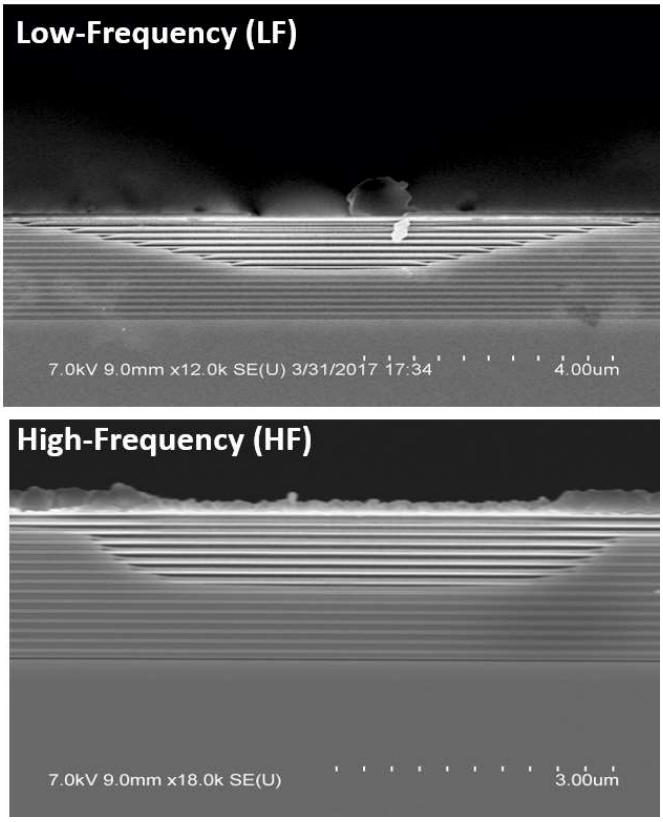

Figure 4.4: Distinctly different IID aperture formed using LF and HF deposited SiN_x films [16].

tify these diffusion fronts, the lateral-to-vertical diffusion ratios are recorded for each IID aperture. This measurement process is shown in Fig. 4.5.

The L/V ratio for LF and HF sourced SiN_x diffusion masked IID apertures were measured to be 3.94 and 1.04 respectively. It is noted that the curvature of these two diffusion fronts are not accurately depicted due magnification differences between the two images. However, if the pictures are scaled to match the same imaging scale, the difference of diffusion front curvatures can be seen to be quite significant as shown in Fig. 4.6.

In addition to the purely HF and LF sourced SiN_x deposited films, 0.70 and 0.90 HF time ratio films were deposited and employed for disordering. These films are shown in the top and bottom of Fig. 4.7 respectively. The L/V ratio for various compositions of SiN_x films is plotted alongside the corresponding film stresses induced on the 2-inch SI GaAs wafer substrate. As seen, the L/V ratio is inversely proportional to the film stress induced by a given diffusion mask. For compressively (negative) strained films, the L/V ratio reaches

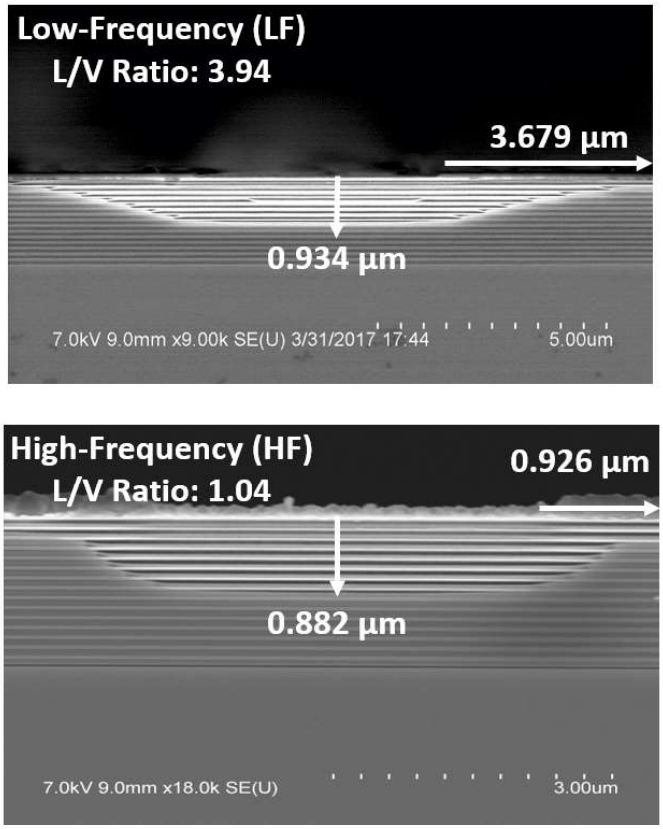

Figure 4.5: Lateral-to-vertical ratio measurement for IID apertures formed with LF (top) and HF (bottom) SiN_x deposited diffusion masks adapted from [16].

a maximum of 4.16 for purely LF-sourced IID apertures. Contrarily, for highly tensile (positive) strained films, the L/V ratio measured a minimum of 0.95 for purely HF-sourced IID apertures. The ranges of L/V ratios for LF- and HF-sourced IID apertures across the various stripe vias formed in each sample was found to be 3.16 to 4.16 and 0.95 to 1.36 respectively.

Figure 4.8 shows that the ranges of L/V ratio for mixed-frequency films 0.70 and 0.90 HF time ratio are measured to be 2.51 to 2.92 and 1.83 to 2.58 respectively. It is noted that the spread of L/V ratios is quite larger, however, this is attributed toward the unaccounted angular tilt and view angle that can lead to slightly wider or narrower diffusion dimensions. It can be seen that the overall trend-line reveals that the L/V ratio montonically decreases in an exponential-like manner with increasing HF time ratio depositions. This suggests that IID aperture designs, which are defined by their L/V diffusion ratios, can be engineered through modifying the diffusion mask

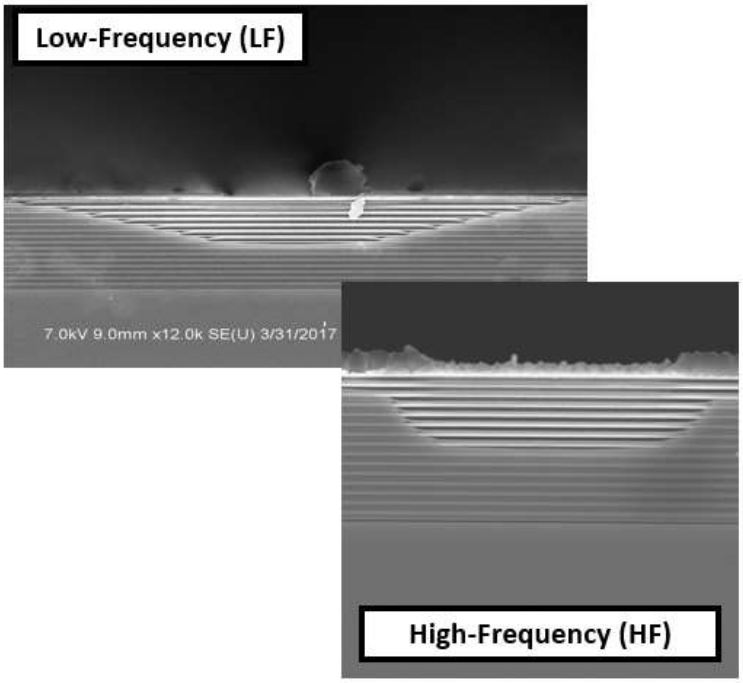

Figure 4.6: HF and LF sourced IID apertures scaled to the same SEM imaging scale for comparison adapted from [16].

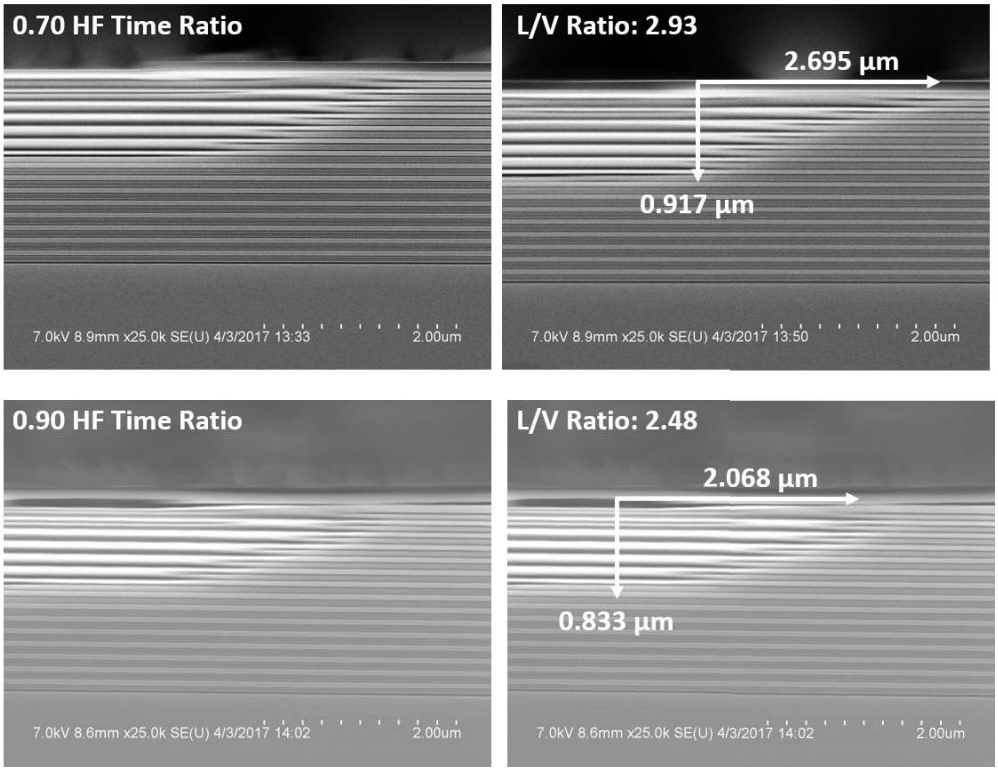

Figure 4.7: IID aperture formed using 0.70 (top) and 0.90 (bottom) HF time ratio composition SiN_x diffusion masks.

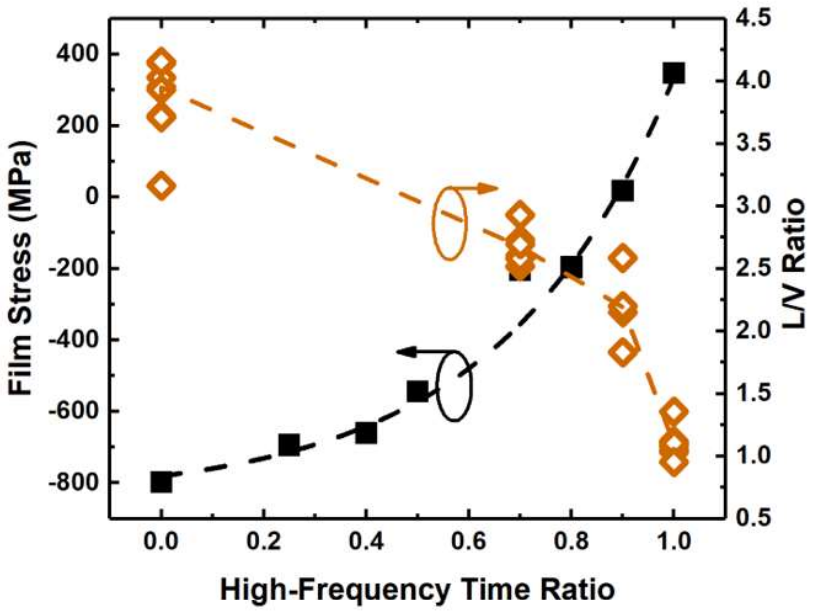

Figure 4.8: The lateral-to-vertical (L/V) diffusion ratio as a dependence of measured film stress [16].

strain induced. This work demonstrates this capability through modifying the high-frequency time ratio of mixed-frequency films, however, the film stress can also be modified through adjusting the gas flows, plasma power, pressure, temperature, and thickness [43, 44, 45].

This experimentally demonstrates the capability to finely control the diffusion front of IID apertures that enables more intricate and application-specific IID aperture designs for optical mode control, higher modulation speeds, and even higher power performance in VCSELs. Further work can be done to extend the capacity of this effect by introducing increasingly tensile strained films.

4.3 Physical Mechanisms of Strain-Controlled Diffusion Front

The physical mechanisms proposed to explain the IID aperture behavior is explained through the theory of biaxial tension strain of cubic lattices. As derived from [36], the lattice-mismatched strain between the SiN_x diffusion mask and the top of the eptiaxial VCSEL sample during disordering can be

approximated as a biaxial strained thin film. This results in the following directional stain matrix components as:

$$\epsilon_{xx} = \epsilon_{yy} = \frac{a_0 - a}{a} \tag{4.3}$$

$$\epsilon_{xy} = \epsilon_{yz} = \epsilon_{zx} = 0 \tag{4.4}$$

$$\epsilon_{zz} = -2\frac{C_{12}}{C_{11}}\epsilon_{xx} = -2\frac{C_{12}}{C_{11}}\epsilon_{yy} \tag{4.5}$$

where a_0 and a are lattice constants of the top VCSEL epitaxial layer and thin film layer respectively while C_{12}, C_{11} are the elastic stiffness tensor elements. As shown in Fig. 4.8, the film stress induced by the LF SiN_x is compresssive while the HF SiN_x induces a tensile strain. Here, compressive and tensile strained films possesses a lattice constant in reference towards the substrate film as the following:

$$\text{Tensile Strain} : a(x) < a_0, \epsilon_{xx} > 0, \epsilon_{zz} < 0 \tag{4.6}$$

$$\text{Compressive Strain} : a(x) > a_0, \epsilon_{xx} < 0, \epsilon_{zz} > 0 \tag{4.7}$$

As a result, with a GaAs lattice constant of 5.65 Å, the effective lattice constants of the amorphous HF and LF sourced SiN_x are smaller and larger respectively. In the tensile strained case, the ϵ_{xx} determined to be positive while the ϵ_{zz} is determined to be negative. In the compressively strained case, this effect is reversed where ϵ_{xx} is determined to be negative and ϵ_{zz} to be positive. This can be interpreted that for the compressively strained case, the lattice atoms of the GaAs layer in the growth direction are pulled slightly further from another. This allows the diffusion of Zn to propagate further laterally due to wider interstitial lanes (in the z-direction) that have weaker coulombic potential effects that decrease proportionally by $\frac{1}{r^2}$. Contrastly, in the tensile strained case, the interstitial diffusion lanes (in the z-direction) are narrower which create a larger potential sites for lateral diffusing Zn; thus making it more difficult for Zn to overcome the larger potential barriers. This model predicts that the LF-sourced SiN_x film would result in a wider

laterally diffused IID aperture while the HF-sourced SiN_x film would result in a narrower laterally diffused IID aperture. This conclusion is in good agreement with the experimental results presented in Fig. 4.4 and Fig. 4.5.

This model, however, can be greatly improved since SiN_x as mentioned is an amorphous film. In which, lattice constants vary across the extent of the film and invoking an effective lattice constant should be replaced for a more rigorous explanation. It is noted that the strain effects induced onto a VCSEL are only present during the disordering process. Once the disordering aperture is formed, the diffusion mask is removed and a conventional oxide-confined VCSEL is fabricated without any strain induced on the top of the device.

CHAPTER 5

CONCLUSION AND FUTURE OUTLOOK

This work motivates, proposes, and demonstrates the capability to control the diffusion front of impurity-induced disordering apertures by modifying the diffusion mask strain. By engineering the strain induced by the diffusion mask through forming various frequency compositions of SiN_x, the diffusion front of the disordering aperture formed into VCSEL DBR can be finely controlled. This has been demonstrated to result in various disordering aperture geometries with an L/V ratio ranging from 0.95 to 4.16 for a diffusion mask strain of + 347 MPa and -797 MPa respectively. This capability enables the formation of improved application-specific IID apertures for improved optical mode control, faster modulation frequency, and higher-power VCSELs.

Future considerations extending this work would be to explore and develop lower L/V ratio IID apertures. Apart from shallow Zn-diffusion for improved current spreading where a large lateral diffusion component may become desirable, the effects of HOM suppression becomes increased for a greater number of disordered pairs. Thus, the capability to from deeper disordering apertures which minimizes lateral diffusion (i.e. low L/V ratio) is beneficial for optical mode control to achieve single-mode performance.

REFERENCES

[1] I. Melngailis, "Longitudinal injection-plasma laser of InSb," *Applied Physics Letters*, vol. 6, no. 3, pp. 59–60, 1965.

[2] H. Soda, K. Iga, C. Kitahara, and Y. Suematsu, "GaInAsP/InP surface emitting lasers," *Japanese Journal of Applied Physics*, vol. 18, pp. 2329–2330, 1979.

[3] D. R. Scifres and R. D. Burnham, "Distributed Feedback Diode Laser," Sep. 28 1976, US Patent 3,983,509.

[4] J. Dallesasse, N. Holonyak Jr, A. Sugg, T. Richard, and N. El-Zein, "Hydrolyzation oxidation of AlxGa1-xAs-AlAs-GaAs quantum well heterostructures and superlattices," *Applied Physics Letters*, vol. 57, no. 26, pp. 2844–2846, 1990.

[5] D. Huffaker, D. Deppe, K. Kumar, and T. Rogers, "Native-oxide defined ring contact for low threshold vertical-cavity lasers," *Applied Physics Letters*, vol. 65, no. 1, pp. 97–99, 1994.

[6] R. Prieto, "Cisco global cloud index projects cloud traffic to nearly quadruple representing 92 percent of total data center traffic by 2020," *Cisco Newsroom*, 2016.

[7] M. P. Li, "Overcome copper limits with optical interfaces," *Altera White Paper*, 2011.

[8] H. Moench, M. Carpaij, P. Gerlach, S. Gronenborn, R. Gudde, J. Hellmig, J. Kolb, and A. van der Lee, "VCSEL-based sensors for distance and velocity," in *Vertical-Cavity Surface-Emitting Lasers XX*, vol. 9766. International Society for Optics and Photonics, 2016, p. 97660A.

[9] A. Börcs, B. Nagy, and C. Benedek, "Instant object detection in LiDAR point clouds," *IEEE Geoscience and Remote Sensing Letters*, vol. 14, no. 7, pp. 992–996, 2017.

[10] M. Miller, M. Grabherr, R. King, R. Jager, R. Michalzik, and K. J. Ebeling, "Improved output performance of high-power VCSELs," *IEEE*

Journal of Selected Topics in Quantum Electronics, vol. 7, no. 2, pp. 210–216, 2001.

[11] H. Moench, "VCSEL arrays provide leading-edge illumination for 3d sensing," *Lase Focus World*, vol. 53, no. 10, pp. 31–33, 2017.

[12] H. Moench, R. Conrads, C. Deppe, G. Derra, S. Gronenborn, X. Gu, G. Heusler, J. Kolb, M. Miller, P. Pekarski *et al.*, "High-power VCSEL systems and applications," in *High-Power Diode Laser Technology and Applications XIII*, vol. 9348. International Society for Optics and Photonics, 2015, p. 93480W.

[13] J. M. Dallesasse and D. G. Deppe, "III-V oxidation: discoveries and applications in vertical-cavity surface-emitting lasers," *Proceedings of the IEEE*, vol. 101, no. 10, pp. 2234–2242, 2013.

[14] K. Iga, "Forty years of vertical-cavity surface-emitting laser: Invention and innovation," *Japanese Journal of Applied Physics*, vol. 57, no. 8S2, p. 08PA01, 2018.

[15] K. Iga and H. Li, *Vertical-Cavity Surface-Emitting Laser Devices*. Springer, 2003.

[16] P. Su, F.-C. Hsiao, T. O'Brien, and J. M. Dallesasse, "Wafer-scale method of controlling impurity-induced disordering for optical mode engineering in high-performance VCSELs," *IEEE Transactions on Semiconductor Manufacturing*, vol. 31, no. 4, pp. 447–453, 2018.

[17] T. O'Brien, B. Kesler, S. Al Mulla, and J. M. Dallesasse, "Mode behavior of VCSELs with impurity-induced disordering," *IEEE Photonics Technology Letters*, vol. 29, no. 14, pp. 1179–1182, 2017.

[18] G. Pan, Y. Xie, C. Xu, M. Xun, Y. Dong, J. Deng, and J. Sun, "Large-scale proton-implant-defined VCSEL arrays with narrow beamwidth," *IEEE Electron Device Letters*, vol. 39, no. 3, pp. 390–393, 2018.

[19] J. K. Guenter, R. A. Hawthorne, D. N. Granville, M. K. Hibbs-Brenner, and R. A. Morgan, "Reliability of proton-implanted VCSELs for data communications," in *Fabrication, Testing, and Reliability of Semiconductor Lasers*, vol. 2683. International Society for Optics and Photonics, 1996, pp. 102–114.

[20] R. Michalzik and K. J. Ebeling, "Operating principles of VCSELs," in *Vertical-Cavity Surface-Emitting Laser Devices*. Springer, 2003, pp. 53–98.

[21] F. Tan, M.-K. Wu, M. Liu, M. Feng, and N. Holonyak, "850 nm oxide-VCSEL with low relative intensity noise and 40 Gb/s error free data transmission," *IEEE Photonics Technology Letters*, vol. 26, no. 3, pp. 289–292, 2014.

[22] P. Westbergh, J. S. Gustavsson, B. Kogel, A. Haglund, A. Larsson, A. Mutig, A. Nadtochiy, D. Bimberg, and A. Joel, "40 Gbit/s error-free operation of oxide-confined 850 nm VCSEL," *Electronics Letters*, vol. 46, no. 14, pp. 1014–1016, 2010.

[23] J. Dallesasse and N. Holonyak Jr, "Oxidation of Al-bearing III-V materials: A review of key progress," *Journal of Applied Physics*, vol. 113, no. 5, p. 5, 2013.

[24] C. Jung, R. Jager, M. Grabherr, P. Schnitzer, R. Michalzik, B. Weigl, S. Muller, and K. J. Ebeling, "4.8 mw singlemode oxide confined top-surface emitting vertical-cavity laser diodes," *Electronics Letters*, vol. 33, no. 21, pp. 1790–1791, 1997.

[25] H. Martinsson, J. Vukusic, M. Grabberr, R. Michalzik, R. Jager, K. J. Ebeling, and A. Larsson, "Transverse mode selection in large-area oxide-confined vertical-cavity surface-emitting lasers using a shallow surface relief," *IEEE Photonics Technology Letters*, vol. 11, no. 12, pp. 1536–1538, 1999.

[26] J. M. Jin, *Theory and Computation of Electromagnetic Fields*. Hoboken, NJ: John Wiley and Sons, 2010.

[27] T. R. O'Brien, "High-power single-mode vertical-cavity surface-emitting lasers via impurity induced disordering," Dec 2017. [Online]. Available: http://hdl.handle.net/2142/99460

[28] P. Debernardi, A. Kroner, F. Rinaldi, and R. Michalzik, "Surface relief versus standard VCSELs: a comparison between experimental and hot-cavity model results," *IEEE Journal of Selected Topics in Quantum Electronics*, vol. 15, no. 3, pp. 828–837, 2009.

[29] D.-S. Song, S.-H. Kim, H.-G. Park, C.-K. Kim, and Y.-H. Lee, "Single-fundamental-mode photonic-crystal vertical-cavity surface-emitting lasers," *Applied Physics Letters*, vol. 80, no. 21, pp. 3901–3903, 2002.

[30] C. J. Chang-Hasnain, Y. Zhou, M. C. Huang, and C. Chase, "High-contrast grating VCSELs," *IEEE Journal of Selected Topics in Quantum Electronics*, vol. 15, no. 3, pp. 869–878, 2009.

[31] D. Zhou and L. J. Mawst, "High-power single-mode antiresonant reflecting optical waveguide-type vertical-cavity surface-emitting lasers," *IEEE Journal of Quantum Electronics*, vol. 38, no. 12, pp. 1599–1606, 2002.

[32] W. Laidig, N. Holonyak Jr, M. Camras, K. Hess, J. Coleman, P. Dapkus, and J. Bardeen, "Disorder of an AlAs-GaAs superlattice by impurity diffusion," *Applied Physics Letters*, vol. 38, no. 10, pp. 776–778, 1981.

[33] D. G. Deppe and N. Holonyak Jr, "Atom diffusion and impurity-induced layer disordering in quantum well III-V semiconductor heterostructures," *Journal of Applied Physics*, vol. 64, no. 12, pp. R93–R113, 1988.

[34] U. Gösele and F. Morehead, "Diffusion of zinc in gallium arsenide: a new model," *Journal of Applied Physics*, vol. 52, no. 7, pp. 4617–4619, 1981.

[35] R. Longini, "Rapid zinc diffusion in gallium arsenide," *Solid-State Electronics*, vol. 5, no. 3, pp. 127–130, 1962.

[36] S. L. Chuang, *Physics of Photonic Devices*. Hoboken, NJ: John Wiley and Sons, 2009.

[37] S. Adachi, "GaAs, AlAs, and AlxGa1-xAs: Material parameters for use in research and device applications," *Journal of Applied Physics*, vol. 58, no. 3, pp. R1–R29, 1985.

[38] A. Munoz-Yague and M. Bafleur, "Shallow defect etching of GaAs using AB solution under laser illumination," *Journal of Crystal Growth*, vol. 53, no. 2, pp. 239–248, 1981.

[39] E. I.-C. Chen, "Selective oxidation of aluminum-bearing III-V semiconductors: Properties and applications to quantum well heterostructure lasers and transistor devices," Jan 1996. [Online]. Available: http://hdl.handle.net/2142/23442

[40] B. Kesler, T. O'Brien, G.-L. Su, and J. M. Dallesasse, "Facilitating single-transverse-mode lasing in VCSELs via patterned dielectric antiphase filters," *IEEE Photonics Technology Letters*, vol. 28, no. 14, pp. 1497–1500, 2016.

[41] P. Asbeck, M.-C. Chang, J. Higgins, N. Sheng, G. Sullivan, and K.-C. Wang, "GaAlAs/GaAs heterojunction bipolar transistors: Issues and prospects for application," *IEEE Transactions on Electron Devices*, vol. 36, no. 10, pp. 2032–2042, 1989.

[42] Y.-R. Yuan, K. Eda, G. A. Vawter, and J. L. Merz, "Open tube diffusion of Zn into AlGaAs and GaAs," *Journal of Applied Physics*, vol. 54, no. 10, pp. 6044–6046, 1983.

[43] K. Mackenzie, D. Johnson, M. DeVre, R. Westerman, and B. Reelfs, "Stress control of Si-based PECVD dielectrics," in *Proceedings of the 207th Electrochemical Society Meeting*, 2005, pp. 148–159.

[44] C. Blaauw, "Stress in chemical-vapor-deposited SiO2 and plasma-SiNx films on GaAs and Si," *Journal of Applied Physics*, vol. 54, no. 9, pp. 5064–5068, 1983.

[45] S. King, R. Chu, G. Xu, and J. Huening, "Intrinsic stress effect on fracture toughness of plasma enhanced chemical vapor deposited SiNx: H films," *Thin Solid Films*, vol. 518, no. 17, pp. 4898–4907, 2010.

[46] G. G. Stoney, "The tension of metallic films deposited by electrolysis," *Proceedings of the Royal Society of London. Series A, Containing Papers of a Mathematical and Physical Character*, vol. 82, no. 553, pp. 172–175, 1909.